

The BM@N spectrometer at the NICA accelerator complex.

S. Afanasiev^a, V. Astakhov^a, V. Babkin^a, D. Baranov^a, S. Bazylev^a, M. Buryakov^a, S. Buzin^a, A. Chebotov^a,
D. Chemezov^a, A. Dmitriev^a, D. Dryablov^a, P. Dulov^{a,1}, A. Egorov^a, D. Egorov^a, A. Fediunin^a, I. Filippov^a,
I. Gabdrakhmanov^a, A. Galavanov^{a,1}, O. Gavrischuk^a, K. Gertsenberger^a, V. Golovatyuk^a, P. Grigoriev^a,
M. Golubeva^c, F. Guber^c, A. Ivashkin^c, A. Izvestnyy^c, M. Kapishin^a, I. Kapitonov^a, V. Karjavin^a, N. Karpushkin^c,
R. Kattabekov^a, V. Kekelidze^a, S. Khabarov^a, Yu. Kiryushin^a, Yu. Kopylov^a, L. Kovachev^{a,1}, I. Kruglova^a, S. Kuklin^a,
E. Kulish^a, V. Kutergina^a, E. Ladygin^a, N. Lashmanov^a, E. Litvinenko^a, A. Makankin^a, A. Makhnev^a, E. Martovitsky^a,
S. Merts^a, S. Morozov^c, R. Nagdasev^a, D. Nikitin^a, S. Novozhilov^a, V. Petrov^a, S. Piyadin^a, S. Reshetova^a, V. Rogov^a,
I. Rufanov^a, P. Rukoyatkin^a, M. Rummyantsev^a, A. Semak^g, A. Sheremetyeva^a, S. Sedykh^a, R. Shindin^a, S. Sergeev^a,
A. Shchipunov^a, A. Shutov^a, V. Shutov^a, I. Slepnev^a, V. Slepnev^a, A. Smirnov^a, T. Smolyanin^a, A. Sorin^a,
V. Spaskov^a, E. Streletskaya^a, N. Tarasov^a, O. Tarasov^a, A. Terletsky^a, V. Tikhomirov^a, A. Timoshenko^a, N. Topilin^a,
V. Velichkov^a, V. Volkov^c, V. Yurevich^a, N. Zamiatin^a, M. Zavertyaev^{d,*}, A. Zinchenko^a, A. Zubankov^c, E. Zubarev^a

^aJoint Institute for Nuclear Research (JINR), Dubna, Russia

^bNational Research Nuclear University MEPhI, Moscow, Russia

^cInstitute for Nuclear Research of the RAS (INR RAS), Moscow, Russia

^dLebedev Physical Institute of the Russian Academy of Sciences (LPI RAS), Moscow, Russia

^eInstitute of Mechanics at the Bulgarian Academy of Sciences (IMech-BAS), Sofia, Bulgaria

^fPlovdiv University "Paisii Hilendarski", Plovdiv, Bulgaria

^gState Research Center - Institute for High Energy Physics (IHEP), Protvino, Russia

Abstract

BM@N (Baryonic BM@N (baryonic matter at Nuclotron)) is the first experiment operating and taking data at the Nuclotron/NICA ion-accelerating complex. The aim of the BM@N experiment is to study interactions of relativistic heavy-ion beams with fixed targets. We present a technical description of the BM@N spectrometer including all its subsystems.

Keywords: Accelerator, beam, heavy ion, fixed target microstrips, calorimeter.

1. Introduction

BM@N (Baryonic Matter at Nuclotron) is the first experiment operational at the Nuclotron/NICA ion-accelerating complex, dedicated to studying interactions of relativistic beams of heavy ions with fixed targets [1] in the energy range that allows reaching high densities of baryonic matter [3]. The Nuclotron will provide the experiment with beams of a variety of particles, from protons to gold ions, with kinetic energy in the range from 1 to 6 GeV/n for light ions with a Z/A ratio of ~ 0.5 and up to 4.5 GeV/n for heavy ions with a Z/A ratio of ~ 0.4 . At such energies, the density of nucleons in the fireball created by two colliding heavy nuclei is 3–4 times higher than the nuclear saturation density [4]. The primary goal of the experiment is to explore the QCD phase diagram in the region of high baryonic chemical potential, to search for the onset of critical phenomena, in particular the conjectured critical end point and to constrain the parameters of the equation of state (EoS) of high-density nuclear matter. In addition, the Nuclotron energies are high enough to study strange mesons and (multi)-strange hyperons produced in nucleus-nucleus collisions close to the kinematic threshold [5, 6]. Studies of the excitation function of strange particle production below and near to the kinematical threshold make it possible to distinguish the hard behavior of the EoS from the soft one [7].

The BM@N detector is a forward spectrometer covering the pseudorapidity range $1.6 \leq \eta \leq 4.4$. A schematic view of the BM@N setup, as used in the first physics run in 2023 with a Xe beam, is shown in Fig. 1. The setup

*Email Address: zavertyaevmv@lebedev.ru

37 comprises a dipole magnet along with several detector systems to monitor the beam, to identify produced charged
 38 particles, to measure their momentum, and to determine the the geometry of nucleus-nucleus collisions. The caption
 39 of Fig. 1 lists the names of the detector systems and the abbreviations used throughout this paper. The details for all
 40 subsystems are given in the corresponding sections below.

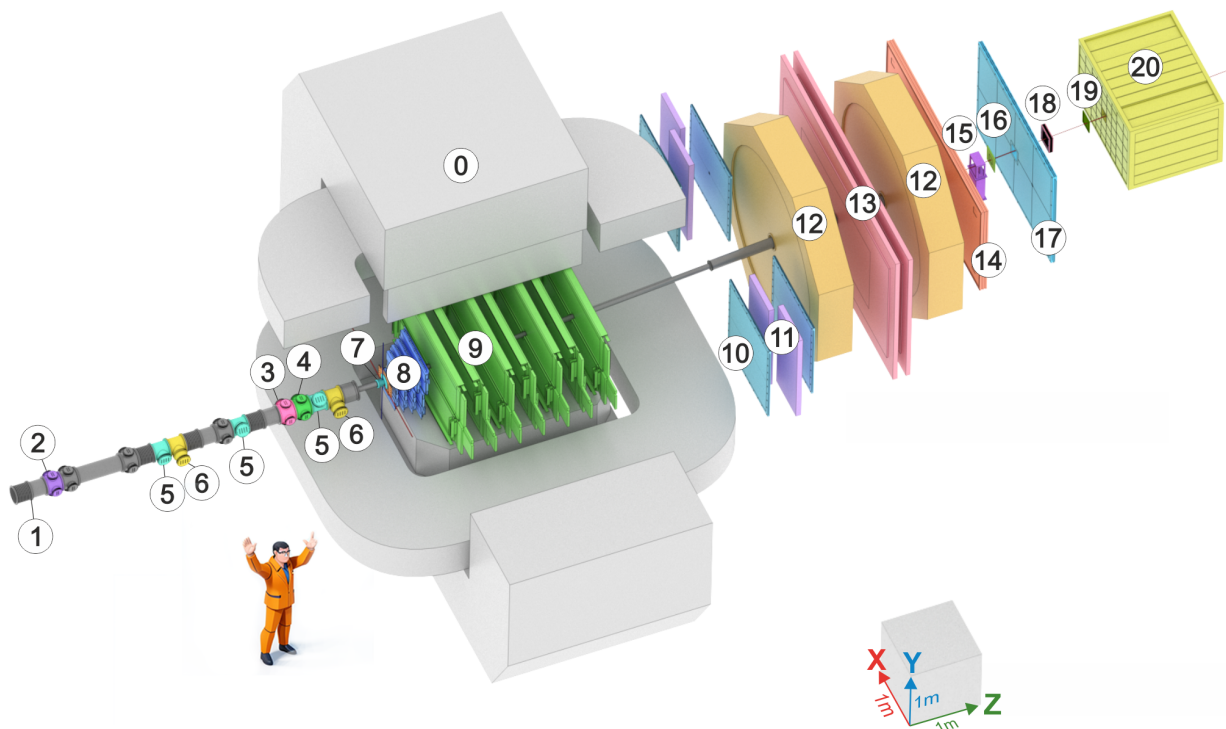


Fig. 1. Schematic view of the BM@N setup in the 2023 Xe run. 0) SP-41 analyzing magnet. 1) Vacuum beam pipe. 2) BC1 beam counter. 3) Veto counter (VC). 4) BC2 beam counter. 5) Silicon Beam Tracker (SiBT). 6) Silicon beam profilometers. 7) Barrel Detector (BD) and Target (TG). 8) Forward Silicon Detector (FSD). 9) Gaseous Electron Multiplier (GEM) detectors. 10) Small cathode strip chambers (Small CSC). 11) TOF400 system. 12) Drift chambers (DCH). 13) TOF700 system. 14) Scintillation Wall (ScWall). 15) Fragment Detector (FD). 16) Small GEM detector. 17) Large cathode strip chamber (Large CSC). 18) Gas ionization chamber as beam profilometer. 19) Forward Quartz Hodoscope (FQH). 20) Forward hadron calorimeter (FHCa).

41 **2. Beamline**

42 **2.1. Beam transport**

43 The BM@N experiment operates as part of the NICA complex (see Fig. 2). NICA facility has two ways for ions
44 acceleration - light and heavy ions. LU-20 is a source of light ions (d-Mg) directly injecting the extracted beam into
45 the Nuclotron accelerating ring. After the acceleration till ??? GeV ions are delivered to application channel, NICA
46 collider, BM@N experimental area.

47 For heavy ion acceleration chain a special ion source and heavy ion linear accelerator (Linac) is a start point. A
48 formed heavy ion beam injects into the Booster ring. Being accelerated up to 500MeV the heavy ion beam may be
49 delivered to applied experimental area or transferred into the Nuclotron accelerator ring for further acceleration up to
50 ??? GeV. At the end heavy ion beam is delivered to NICA Collider.

51 At Collider facility two experimental area are reserved for two major experiments - Multipurpose Particles Detector
52 (MPD) and Spin Particle Detector.

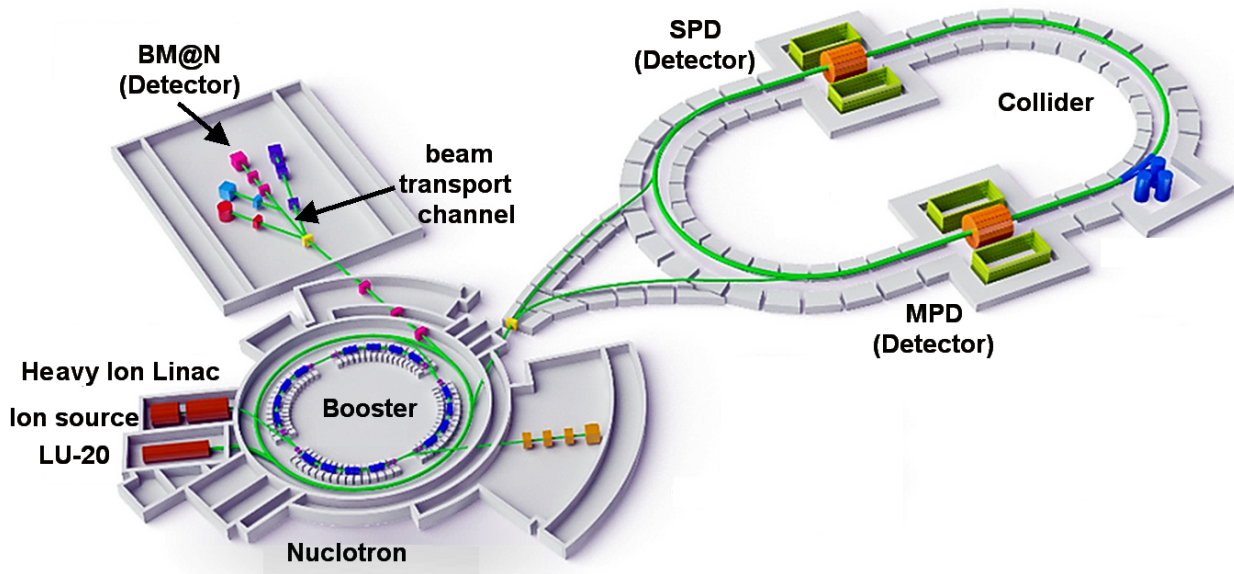


Fig. 2. NICA Complex.

53 The beam extracted from the Nuclotron is transported to the BM@N experimental area over a distance of about
54 150 m by a set of dipole magnets and quadrupole lenses. The transport line is enclosed in a vacuum pipe. At the
55 entrance of the BM@N setup the position and direction of the beam are already close to those required to bring
56 the beam to the target, and only relatively small adjustments are needed to provide final steering of the beam. These
57 corrections are performed by a pair of VKM and SP-57 dipole magnets, which allow bending in vertical and horizontal
58 planes and have a maximum current of 250 A and 600 A, respectively. The centers of these magnets are positioned at
59 approximately 7.7 and 5.7 m from the target (Fig. 3). In addition, a doublet of quadrupole lenses, 1K200 and 2K200,
60 each having a maximum current of 2500 A, allows optimal focusing of the beam on the target. The corresponding
61 position of their centers is at about 12.5 and 10.0 m upstream of the target, respectively.

62 The target is located inside the SP-41 analyzing magnet closer to its entrance. Therefore, after passing through
63 the target, the beam ions are deflected by the SP-41 magnetic field ($\int Bdl = 3.15 Tm$ at the maximum current of
64 2000 A). It should be noted that for experiments with heavy ions, it is essential to have vacuum in the beam line,
65 including the part that goes through the analyzing magnet. This requirement, combined with the need to precisely
66 locate the tracking detectors inside the SP-41, does not allow a quick reconfiguration of the detectors for different
67 beam energy, making it necessary to adjust the magnetic field of the analyzing magnet depending on the choice of the
68 beam energies. Studies of the Xe + CsI collisions during the 2023 Xe run were performed at Xe beam energies of
69 3.0 GeV/n and 3.8 GeV/n, and the current of the SP-41 was set to 1395 and 1720 A respectively.

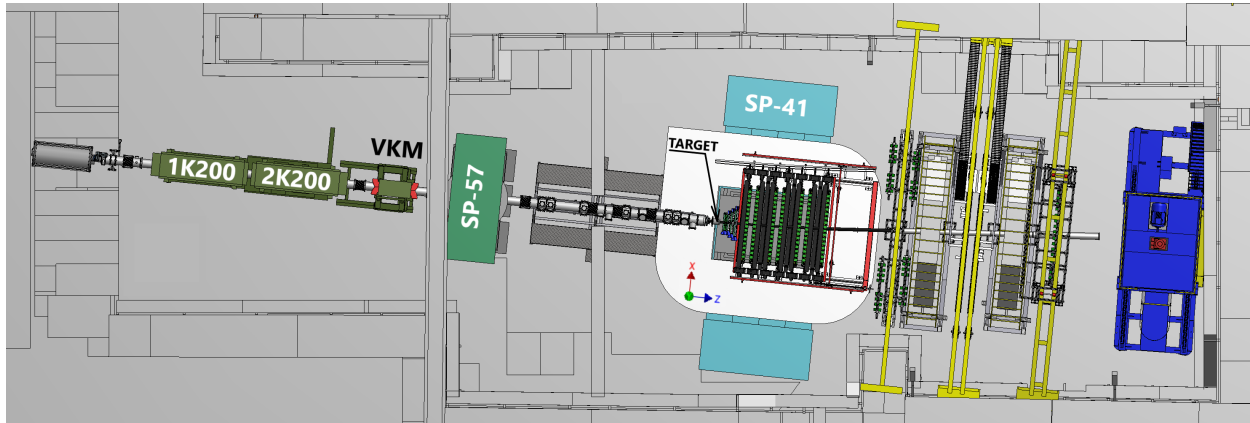


Fig. 3. Magnetic elements of the BM@N setup. See text for details.

2.2. Vacuum beam pipe

A vacuum beam pipe was integrated into the experimental setup in order to minimize the amount of scattering material in the path of the heavy ion beam. The beam pipe has continuous vacuum, but in terms of components and material, the pipe can be subdivided into four large parts. The first section covers the region upstream of the SP-57 magnet inside the magnet itself. The second section goes up to the target. The third section is placed inside the SP-41 analyzing magnet. The last section is located after the analyzing magnet. Vacuum in the entire beam pipe at the BM@N setup is achieved by a single roots pump installed upstream of the 1K200 quadrupole lens. The pressure maintained during the experiment is at the level of 10^{-4} Torr. With the exception of the third part, the configuration of vacuum pipe and its components were designed, manufactured and tested by LLC Vacuum Systems and Technologies (Belgorod, Russia). The ISO-K vacuum standard is adopted for flange connections. However, a significant fraction of the components was custom made in order to meet limitations posed by the magnet size and detector geometry.

The first part of the beam pipe is designed to create vacuum in the area of beam transport through the 1K200 and 2K200 quadrupole lenses and through the VKM and SP-57 corrective magnets. This part of the vacuum pipe is made of stainless steel, has a length of about 12 m and an outer diameter of 200 mm. Two slide gates are installed in this section, one in front of the 1K200 lens and the other after the VKM magnet. The vacuum level is monitored by two vacuum gauges, the data from which are recorded in the Slow Control System.

The second part of the beam pipe serves to create vacuum in the region between the SP-57 magnet and the target located inside the SP-41 magnet. This part of the beam pipe is approximately 5 m long and has an outer diameter of 200 mm. It includes vacuum boxes containing beam detectors described in the next section: two 3-way boxes for profilometers, three 3-way boxes for the Silicon Beam Tracker detectors and three 6-way boxes for the BC1, BC2, and VC trigger counters. All boxes located outside the magnetic field of the SP-41 analyzing magnet are made of stainless steel, while the vacuum pipe components, which have to be close to the target and therefore placed in the magnet, are made of aluminum. The bending of the beam ion trajectories by the magnetic field leads to a deflection from a straight line resulting in a few mm displacement in the X direction at the target location. During the assembly of the beam pipe vacuum elements, an adjustment is carried out in order to compensate for this deflection. For that purpose, the corresponding grooves for the vacuum box O-rings are made slightly wider than dictated by the ISO standard and allow for slight off-center shifts of the vacuum pipe components. The target flange assembly is also made of aluminum as well as a vacuum adapter ISO 240 to 66 mm that provides connection with the vacuum tube of the third section.

The third part of the beam pipe is 4.5 m long and made of carbon fiber. The entire carbon pipe consists of four straight sections of different lengths connected to each other by flangeless carbon fiber connections, which provide the possibility to align sections at slight angles with respect to each other as shown in Figs. 4 and 5. The carbon beam pipe is suspended on two supports also made of carbon fiber and installed on two lower GEM detectors, the one closest to the target and the most downstream one. The supports have adjustment units for precise positioning of the carbon beam pipe on the beam axis (Fig. 5). The carbon beam pipe is designed to sustain vacuum up to 10^{-4} Torr. In the straight segments the thickness is about 1 mm, while in flangeless connections it reaches 2 mm.

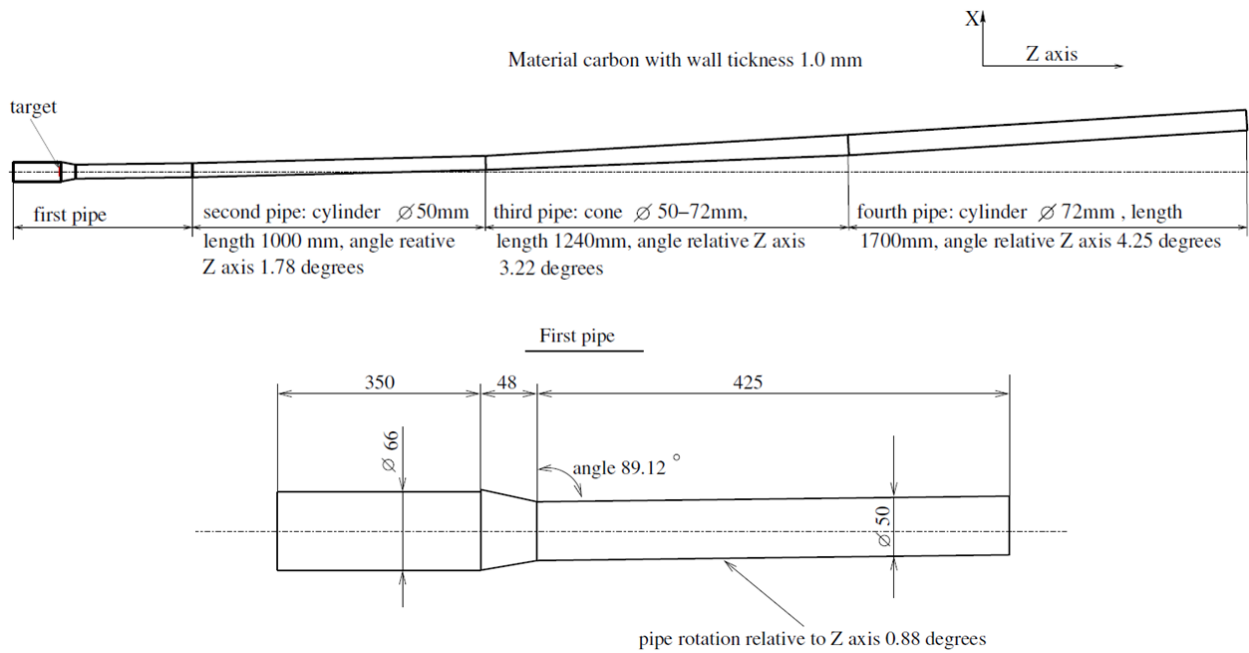


Fig. 4. Technical design of the carbon beam pipe.

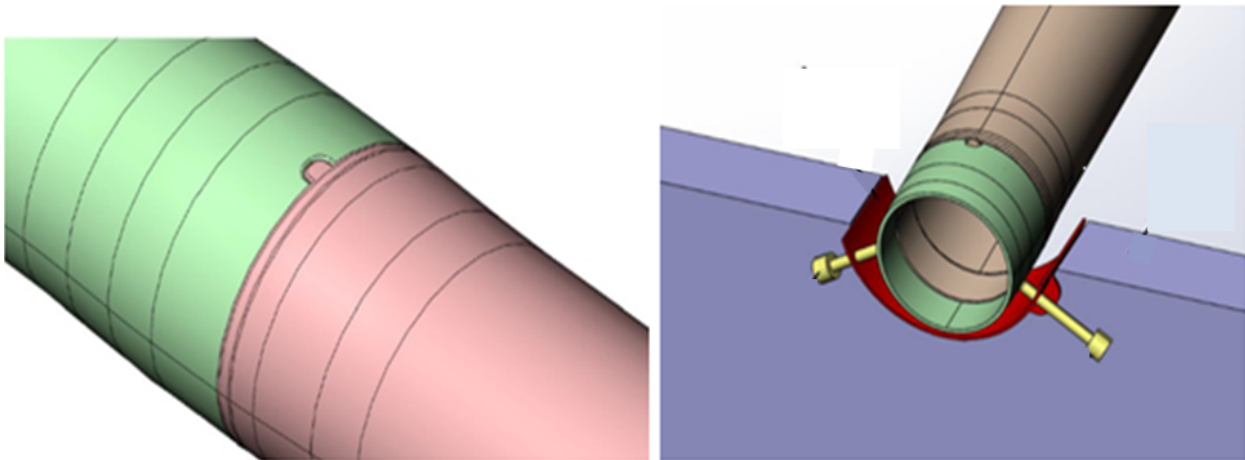


Fig. 5. 3D models of the dismountable flangeless connection (left) and the support scheme of the carbon beam pipe in the GEM detector notch (right).

105 The fourth part of the beam pipe provides vacuum volume along the beam trajectory through the Outer Tracker
 106 system. The pipes and flanges of this section, as well as the connection to the carbon beam pipe, are made of
 107 aluminum. It has an overall length of about 3.2 m and consists of three cylindrical segments with lengths of 1.2,
 108 0.96 and 1.0 m, from the tube with an outer diameter of 125 mm and a wall thickness of 1.5 mm. At the end of this
 109 section, the overall vacuum line is closed by a 100 μm thick titanium membrane installed in a frame after an adapter
 110 ($d = 125/150 \text{ mm}$).

111 *2.3. Target station*

112 The target station is located at the end of the second beam pipe section. It is designed to provide the possibility
113 to insert a target in the beam line inside the vacuum volume and to interchange several targets without breaking the
114 vacuum. A 3d model of the target station is presented in (Fig. 6). An aluminum flange of 240 mm in diameter serves
115 as a holder of the target assembly elements and as an adapter between the beam pipe upstream of the target station
116 and the first section of the carbon beam pipe. On the outer part of this flange, four pneumatic cylinders are installed
117 allowing four target frames to be alternately moved in and out of the beam. The pneumatic cylinders are produced
118 by FESTO and allow remote operation. An optocoupler sensor is used to control the target position via a dedicated
119 electronic module.

120 The part of the target assembly placed inside the vacuum can be divided into three components:

- 121 1) A centering frame, which fits into the inner part of the first section of the carbon beam pipe.
- 122 2) Four petals, in which the targets themselves are installed. In the normal state, all the petals are leaning along
123 the axis direction of the beam pipe.
- 124 3) Carbon fiber retaining pins, 300 mm long and 3 mm in diameter.

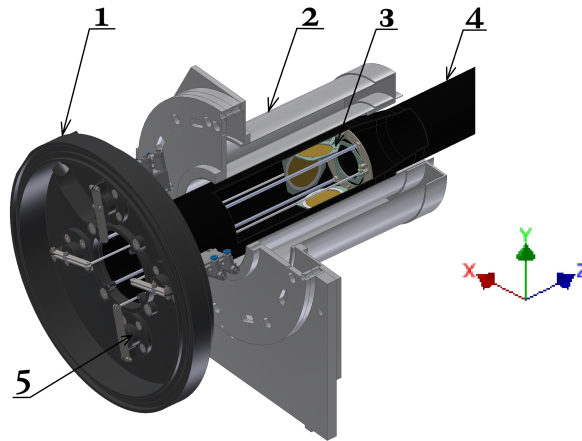


Fig. 6. 3D model of the target station. 1) Aluminum flange target station. 2) Barrel Detector. 3) Four targets. 4) Carbon beam pipe. 5) Pneumatic cylinders.

125 In the 2023 Xe run, three disk targets with a diameter of 3.2 cm were used: 1.75 mm thick CsI, 0.85 mm thick CsI,
126 and 1.02 mm thick Ge. One frame of the target assembly was left empty and was used to evaluate the background
127 level caused by the interaction of beam particles with the structural elements of the target station.

128 *2.4. Magnetic field of the analyzing magnet*

129 The SP-41 dipole magnet with large acceptance is used in the spectrometer as an analyzing magnet to measure the
130 momenta of produced particles and beam fragments. During the preparation of the magnet for the BM@N experiment,
131 the original configuration of the SP-41, used in previous experiments with a streamer chamber, was significantly
132 upgraded. In particular, the camera hole in the upper pole was filled with steel to improve the uniformity of the
133 magnetic field, and the distance between the poles was increased by approximately 30 cm to provide the space required
134 by the BM@N GEM chambers. The dimensions of the SP-41 pole in X and Z directions are about 1.4 and 2.5 m,
135 respectively, while the vertical distance between the upper and lower poles after the upgrade is 1.07 m (Fig. 7). In
136 the BM@N setup, the magnet is roughly centered on the beam line. In the X coordinate the beam axis goes through
137 the magnet close to the center of the poles, while vertically the beam axis is shifted closer to the lower pole by
138 approximately 40 mm. The leading edge of the pole defines the origin of the Z axis, and, correspondingly, the target
139 is installed inside the SP-41 magnet at this position.

140 Determination of the momentum of the produced particles requires a detailed knowledge of the value and orien-
141 tation of the magnetic field. After the upgrade of the SP-41, field measurements were performed by means of planar

142 and 3D Hall probes [8]. In addition, the shape of the field was calculated by the TOSCA code using the known
 143 configuration of the yoke and coils material. Prior to the 2023 Xe run, the magnetic field measurement was repeated
 144 with the goal to obtain the field map for a wider X, Y, Z range and with smaller steps. The measurements with 3D Hall
 145 probes covered $(-156, +145 \text{ cm})$, $(-38, +54 \text{ cm})$, $(-162, +439 \text{ cm})$ and were performed in $(126 \times 47 \times 241)$ points in
 146 X, Y, Z coordinates, respectively, allowing one to construct the field map on a $2.4 \times 2.0 \times 2.5 \text{ cm}^3$ three-dimensional
 147 grid (Fig. 7). During simulation and event reconstruction, the magnetic field components in a particular (x, y, z) point
 148 are calculated by linear interpolation over eight neighboring measured nodes.

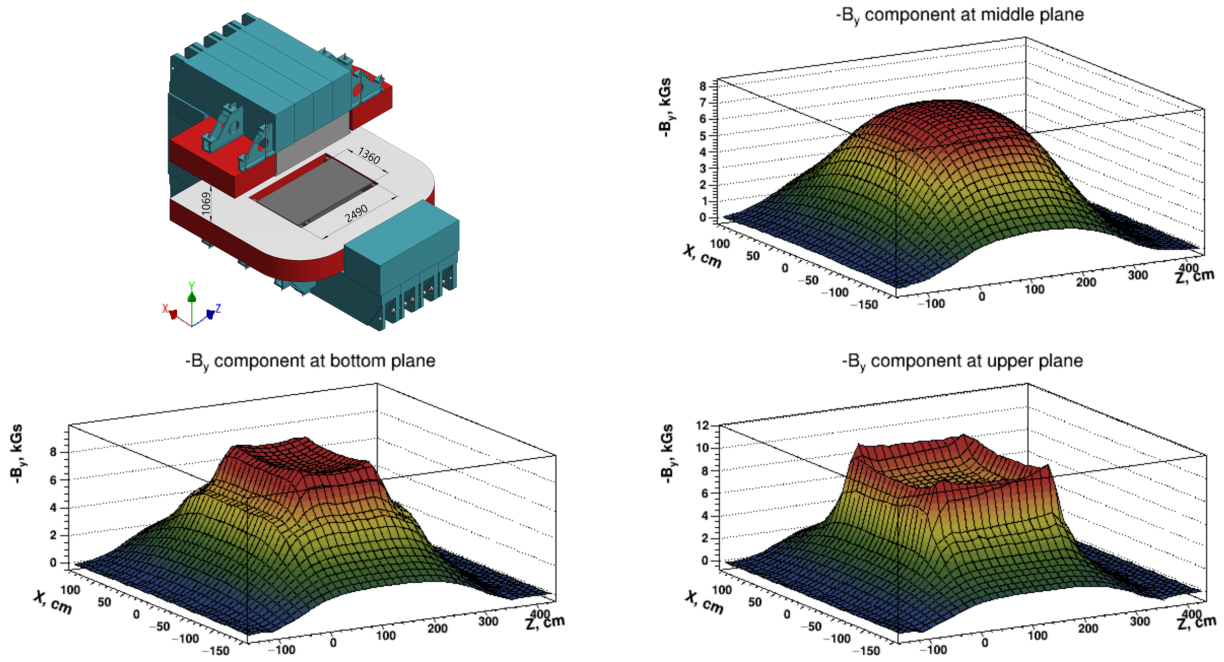


Fig. 7. Magnetic field map of the SP-41 analyzing magnet.

149 The measurements of the field map were performed for four values of the current: 900, 1300, 1600, and 1900 A.

150 **3. Beam and trigger detectors**

151 Fig. 8 shows a schematic layout of the trigger detectors, placed on the beam line. In the target area the multiplicity
 152 Barrel Detector is also shown as a part of the trigger system.

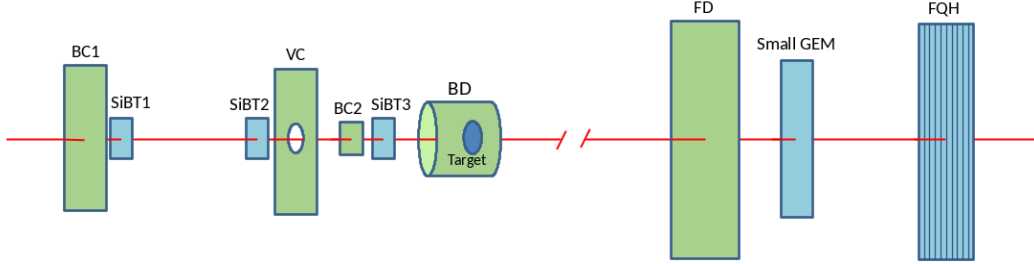


Fig. 8. Beam, trigger, and fragment detector layout.

153 Some physical parameters of the beam line detectors are summarized in Table 1.

154 The beam aperture is limited by the 25 mm diameter hole in the scintillation Veto Counter (VC), which rejects the
 155 beam halo. The diameter of the hole in the VC is chosen to be large enough to accept most of the beam ions, but
 156 smaller than the target diameter of 32 mm. Typically, in the 2023 Xe run, 80 % of the beam was accepted by the VC.
 157 In order to minimize interactions upstream of the target, the scintillators and active parts of the silicon detectors are
 158 located in vacuum, while the photomultiplier tubes (PMTs) of the scintillation counters and the front-end electronics
 159 of the silicon detectors are kept in the air with their housings mounted to the flanges of the beam pipe.

Table 1. Beam line detectors.

Detector	Z position, cm	Active area, mm × mm	Material	Thickness, mm
BC1	-422	100 × 100	Scint. BC400B	0.25
SiBT1	-283	61 × 61	Silicon	0.175
SiBT2	-183	61 × 61	Silicon	0.175
VC	-124	113 × 113 (hole ∅25)	Plastic Scint.	4
BC2	-104	34 × 34	Scint. BC400B	0.15
SiBT3	-84	61 × 61	Silicon	0.175
FD	+784	150 × 150	Scint. BC408	0.5
Small GEM	+793	100 × 100		
FQH	+970	160 × 160	Quartz	4

160 In all the beam scintillation counters - BC1, BC2 and VC - light from the scintillator is collected by Al-mylar light
 161 guides to a pair of PMTs, placed above and below the scintillator. This orientation of the PMTs in the BC2 and VC
 162 detectors is dictated by the requirement that they should operate in the magnetic field of the analyzing magnet, since
 163 they are located close to the target. Hamamatsu R2490-07 mesh dynode PMTs are used in the BC1 and VC detectors,
 164 whereas the BC2 has Photonix XPM85112/A1 Q400 microchannel plate PMTs.

165 The BC1 and BC2 detectors define the start time for the time-of-flight system. The requirement to obtain precise
 166 time measurement favored the design of the BC1 and BC2 with light collection by two PMTs, whereas the input in
 167 the trigger logic is configured to accept one pulse from each of the beam counters, the BC1, BC2, and VC. Individual
 168 signals from the top or bottom PMT are affected by light collection non-uniformity to a larger degree than the summed

169 signal from the individual PMTs. Therefore, the signals from individual PMTs are split by fast fan-out modules, one
170 output of which is used to form the summed pulse for the trigger logic, while the signals from the other output are fed
171 to a TQDC module for offline processing of the individual pulses. Both types of PMTs used in the beam counters,
172 Hamamatsu R2490-07 and Photonis XPM85112/A1 Q400, have excellent timing characteristics. The fan-outs have
173 a time jitter of about 10 ps and preserve the high quality of the time response. After offline correction for time walk
174 (slewing), the time resolution obtained in the 2023 Xe run using pulses from top and bottom PMTs was found to
175 be $\sigma_t \approx 40\text{ ps}$ for the BC1 and BC2 individually, and $\sigma_t \approx 30\text{ ps}$ for the combined response of the system of two
176 counters.

177 Upstream of the target the beam position is traced by three double-sided silicon strip detectors. These detectors
178 are kept permanently in the beam and provide information about the beam ion trajectory for each event. A detailed
179 description of the Silicon Beam Tracker (SiBT) is given in the next chapter. In addition to the SiBT, the beam position
180 and profile can also be measured by a pair of beam profilometers, which are similar in design and parameters to the
181 SiBT stations, but have a much coarser pitch of 1.8 mm in X and Y . The readout of the profilometers is organized
182 independently of the main BM@N DAQ in order to facilitate beam tuning at the early stages of the run. The detectors
183 of the beam profilometers can be moved in and out of the beam by remotely controlled drivers without breaking the
184 vacuum. During data taking, the detectors of the beam profilometers are positioned outside of the beamline.

185 The trigger signal based on the multiplicity of particles produced in the interaction is provided by the Barrel
186 Detector (BD), which is formed by 40 scintillator strips covering a cylindrical surface $\sim 90\text{ mm}$ in diameter oriented
187 along the beam line. Each BD strip has a size of $150 \times 7 \times 7\text{ mm}^3$, is viewed from one side by a $6 \times 6\text{ mm}^2$ silicon
188 photomultiplier (SensL, J-ser.), and is coated with aluminized mylar. The target is situated inside the BD, centered
189 in the XY plane and longitudinally placed at a distance of 35 mm from the downstream edge of the BD strips. This
190 position of the BD is dictated by the requirements for the detector to cover a sufficiently large solid angle while leaving
191 free the acceptance of the tracking detectors of the spectrometer.

192 The δ -electrons generated by beam ions in the target and curved by the magnetic field can significantly contribute
193 to the number of fired strips in the BD. In order to reduce this background, the scintillator strips are protected by
194 Pb-shielding: a 3 mm thick cylinder inside the BD and a 10 mm thick outer plate.

195 Downstream of the analyzing magnet the beam goes through the Fragment Detector (FD), the Small GEM detector
196 and the Forward Quartz Hodoscope (FQH). These detectors are placed in the air, the FD is positioned right after the
197 $100\text{ }\mu\text{m}$ titanium window of the vacuum beam pipe. The amplitude of the pulse in the FD reflects the charge squared
198 of the ion passing through the counter. This amplitude is used in the trigger system in order to distinguish events with
199 and without interactions in the target. To minimize the background from interactions within the FD itself, its radiator
200 has to be thin, while in the X and Y directions the radiator should be wide enough to cover all the beam ions going
201 through the target without interaction. In the 2023 Xe run, the radiator made of a 0.5 mm thick BC408 scintillator
202 was viewed by a single Hamamatsu R2490-07 PMT placed about 50 cm below the beam line. Light collection was
203 done by an air light guide made of aluminized mylar. The pulse height resolution for the Xe peak was found to be
204 $\sigma \approx 5.2\%$.

205 In addition to the FD, the beam ions or spectator fragments can be detected by a 4 mm thick quartz hodoscope
206 FQH located in front of the beam hole in the FHCAL. Information from this hodoscope is used in the offline analysis
207 for event selection and determination of event centrality. The FQH amplitude resolution for Xe ions is about 2% . The
208 detailed description of the hodoscope is given in section 8.2.

209 The small GEM detector is placed between the FD and FQH and used to monitor the position, shape and spot size
210 of the beam downstream of the analyzing magnet. Its active area covers $10\text{ cm} \times 10\text{ cm}$ in X and Y . The detector has
211 three GEM foils and a multilayered readout board with two planes of parallel strips oriented along the X and Y axes
212 with 256 strips in each coordinate.

213 **4. Silicon Beam Tracker**

214 The main task of the Silicon Beam Tracker (SiBT) is to measure the beam ion trajectory in each event and deter-
215 mine the primary vertex coordinates as well as the impact angle of the beam projectile. The SiBT consists of three
216 stations, each of which utilizes a double-sided silicon strip detector (DSSD) with dimensions of $63 \times 63 \times 0.175 \text{ mm}^3$.
217 The DSSDs are made of high-resistivity silicon wafers obtained by the Float Zone method. The detector thickness
218 of $175 \mu\text{m}$ was chosen as small as possible, taking into account the limitations of the planar technology applied to
219 4" (100 mm) wafers. The minimum thickness of the detectors allows not only reducing the amount of material in
220 the beam, but also decreasing the volume of the space charge region of the detector. Thus, the noise caused by the
221 radiation damage per strip is lowered. This is very important considering that the detectors are exposed to heavy ion
222 beams of high intensity.

223 Each detector has an active area of $61 \times 61 \text{ mm}^2$, 128 strips on both the p^+ and the n^+ sides with a pitch of $470 \mu\text{m}$
224 and a spacing of ????? between adjacent strips, resulting in total 2×128 readout channels. The strips on the two
225 sides are oriented orthogonally with respect to each other. The silicon plate in the SiBT1 detector is positioned inside
226 the beam pipe such that the strips are aligned along the X and Y axes, whereas the plates of the SiBT2 and SiBT3
227 detectors are rotated azimuthally by 30° and 60° , respectively.

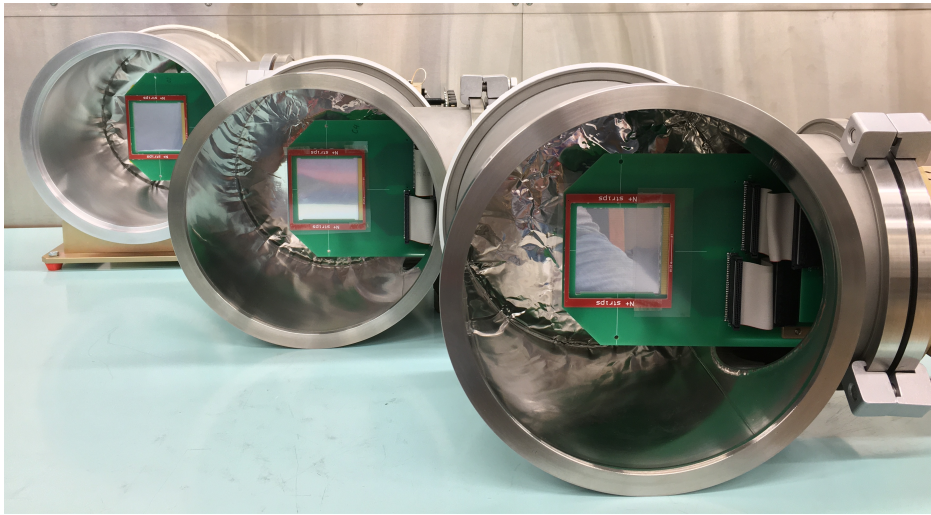


Fig. 9. Three stations SiBT1, SiBT2, SiBT3 with detectors and FEE electronics, view along the beam (n^+ side of the strips).

228 Fig. 9 shows the three vacuum stations with the DSSD installed inside. The 3d coordinate positions of each DSSD
229 relative to the geometrical axis of the beam pipe were measured using a NORGAU NVM II-5040D video meter with
230 an accuracy of $\pm 5 \mu\text{m}$. Structurally, the detectors are assembled on printed circuit boards with gold contact pads,
231 which are connected by ultrasonic bonding (US-bonding) with Al-plated strips on the DSSD. The signals from the
232 detector strips, grouped in four bundles of 64 channels each, are sent via flat cables to 4 vacuum connectors fixed on
233 the vacuum flange. The front-end electronics (FEE) for 128 p^+ and 128 n^+ strips are mounted on the flange outside
234 the vacuum volume. The detector electronics in this case are practically outside of the high radiation zone and are
235 available for testing and, if needed, replacement, without breaking the vacuum in the beam pipe.

236 This chip is VATA64HDR16.2 (IDEAS, Norway), chosen for the FEE because of its large dynamic range ($-20 pC -$
 237 $+50 pC$) suitable for operation with highly ionizing heavy ion beams. For example, the charge in the input signal
 238 caused by $3-4 GeV/n$ Xe ion going through a $175 \mu m$ layer of silicon is $11 pC$.

239 The ASIC VATA64HDR16.2 accepts up to 64 input channels. Therefore, four chips are used in each SiBT stations.
 240 After passing through the pulse shapers, at the time defined by “external trigger - SH”, the values of signal amplitudes
 241 from 64 strips are stored in memory capacitors. After that, in sequential reading mode using an analog multiplexer, the
 242 64 signals are transmitted for digitization into a single ADC channel. The main parameters of the VATA64HDR16.2
 243 chip are given in Table 2.

244 Fig. 10 shows the three SiBT stations mounted in the vacuum beam pipe. The histograms at the bottom part of the
 245 figure represent the online monitoring of the 2D distribution of beam ion hits in the SiBT. The typical RMS of
 246 the beam profile in the 2023 Xe run, measured for trigger selected events, i.e., for ions passing through the $2.5 cm$
 247 diameter hole of the Veto counter, was $0.5 cm$ and $0.6 cm$ in the X and Y coordinates, respectively.

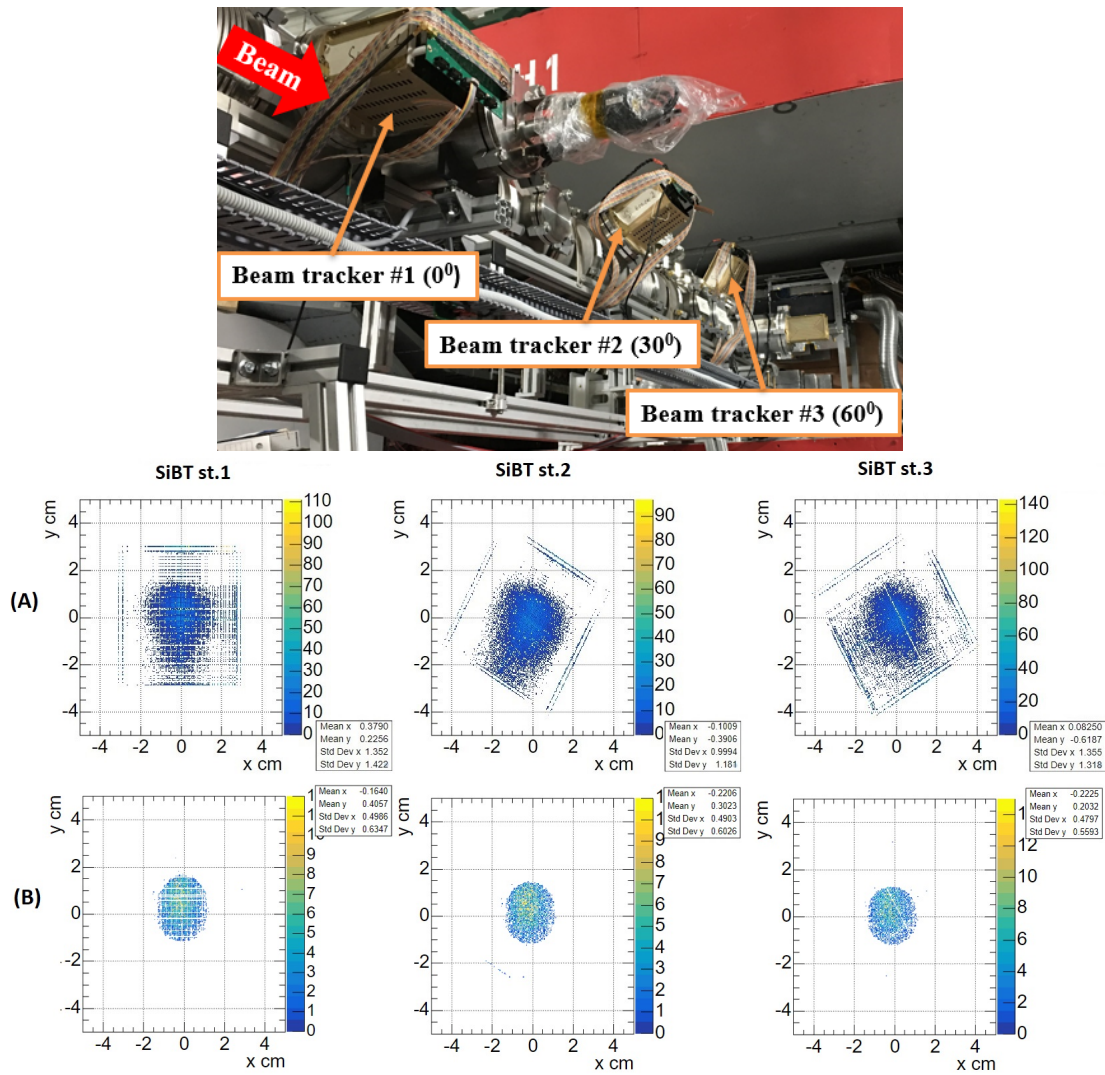


Fig. 10. Top: The three SiBT stations installed in the vacuum beam pipe. Bottom: two-dimensional beam profiles measured in the 2023 Xe run: A) without a Veto counter in the trigger; B) with a Veto counter in the trigger.

248 **5. Central Tracking System**

249 The Central Tracking System (CTS) is based on two large tracking detector systems placed inside the SP41
 250 analyzing magnet. These systems are the Forward Silicon Detector (FSD) located right behind the target area and a
 251 set of Gaseous Electron Multiplier (GEM) detectors installed downstream, inside the interpole volume. The FSD has
 252 four tracking planes, while the GEM system consists of seven tracking planes. In order to accommodate the beam
 253 vacuum pipe going through the setup, each tracking plane in both systems is divided in two half-plane detectors, an
 254 upper and a lower one.

255 The detector position and configuration of the CTS in the 2023 Xe run is shown in Fig. 11 and Fig. 12. A detailed
 256 description of each tracking subsystem is given below.

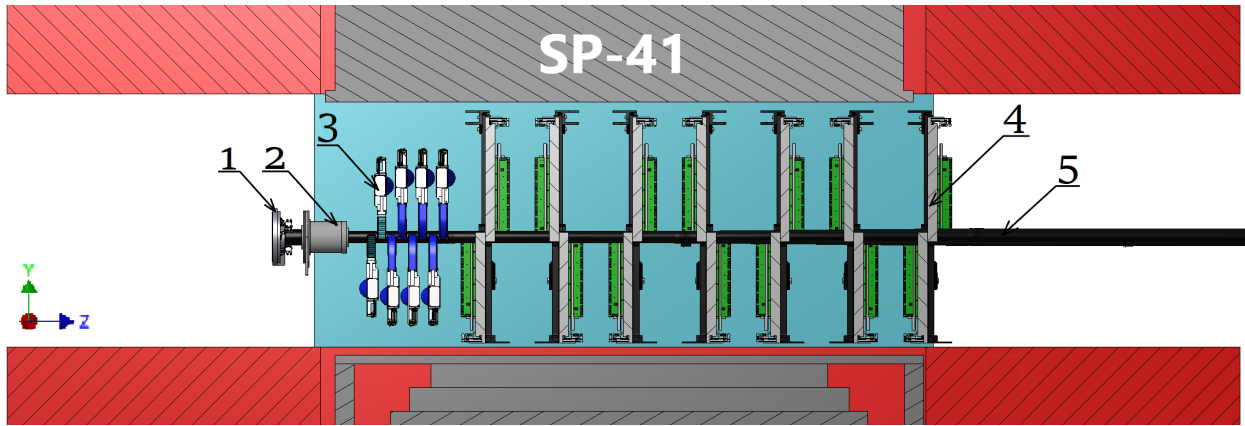


Fig. 11. Side view of the subsystems inside the SP41 analyzing magnet. 1) Target station. 2) Barrel Detector. 3) Forward Silicon Detector. 4) GEM detectors. 5) Beam pipe.

Table 2. Main parameters of the Central Tracking System.

Type of detector	Si- DSSD (175 μm)	Si- DSSD (300 μm)	GEM
Type of chip	VATAG64HDR16	VATAGP 7.1	IDE1163
N_{ch}	64	128	32
Dynamic range (AC)	-20 pC \div + 50 pC	\pm 30 fC	\pm 750 fC
t_s	50ns, 100ns, 150ns, 300 ns, programmable	500 ns	500 ns
$\sigma_0(C_{in} = 0)$	1 fC	70 e	1069 e
P, mW	960 mW	280 mW	77 mW
Detector signal range	\pm 15 pC	\pm (0.5 \div 20) fC	(20 \div 100) fC
Manufacturer's company	IDEAS (Norway)		

257 **5.1. Forward Silicon Detector**

258 Each half-plane of the FSD forms an independent detector incorporating the following systems: coordinate mod-
 259 ules based on DSSD, electronics cross-board, suspension and precise positioning mechanics, cable patch panel, air
 260 cooling, temperature monitors, light and EM shield. The top and bottom halves of each plane are made structurally
 261 identical and interchangeable. In addition, the design allows vertical shift of the half-planes during assembly in order
 262 to provide the possibility to mount/dismount the planes regardless of the installed beam pipe and to minimize the
 263 chances of its mechanical damage. In the working position, the upper and lower half-planes form a single coordinate
 264 system with active regions overlapping along the Y coordinate. In the center of each plane there is an insensitive

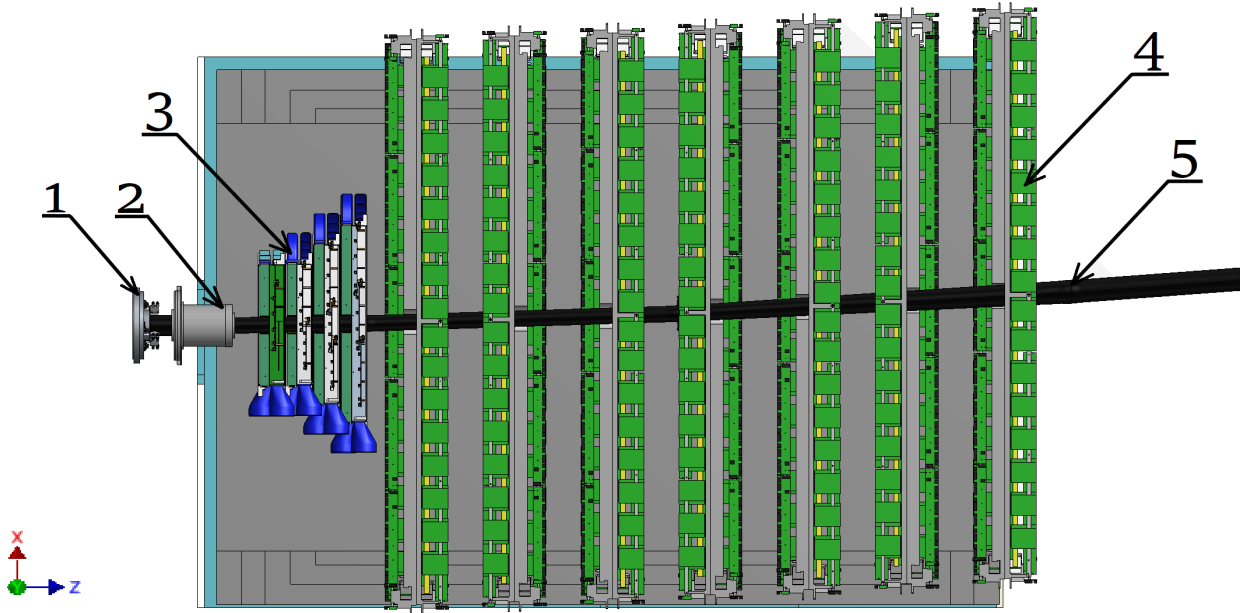


Fig. 12. Top view of the subsystems inside the analyzing magnet. 1) Target station. 2) Barrel Detector. 3) Forward Silicon Detector. 4) GEM detectors. 5) Beam pipe.

265 $57 \times 57 \text{ mm}^2$ zone which makes room for the beam pipe. A top view of the assembled eight half-planes around the
 266 beam pipe inside the SP-41 magnet is shown in Fig. 13.

267 The first plane consists of 6 modules, each of which uses one DSSD with dimensions of $93 \times 63 \times 0.32 \text{ mm}^3$
 268 positioned in such a way that the long side is aligned with the Y coordinate. The detector modules of the remaining
 269 three coordinate planes use two $63 \times 63 \times 0.32 \text{ mm}^3$ DSSDs mounted on a common frame with an accuracy of $\pm 20 \mu\text{m}$.
 270 There, the strips of the same type of one DSSD are connected to the strips of another DSSD by US-bonding with
 271 an aluminum wire of $25 \mu\text{m}$ in diameter. Table 3 provides information about the number of modules and electronic
 272 components in each FSD plane.

Table 3. Main parameters of the Forward Silicon Detector.

Parameters	1 st plane	2 nd plane	3 rd plane	4 th plane	Total
Number of Si- modules	6	10	14	18	48
Number of DSSDs	6	20	28	36	90
DSSD size, mm^2	93×63	63×63	63×63	63×63	
Number of ASICs	60	100	140	180	480
Number of PAs	12	20	28	36	96
Number of FEE PCBs	12	20	28	36	96
Number of channels	7680	12800	17920	23040	53760
Area, m^2	0.035	0.073	0.102	0.132	0.307

273 The $63 \times 63 \times 0.32 \text{ mm}^3$ and $93 \times 63 \times 0.32 \text{ mm}^3$ DSSDs were manufactured at RIMST (Zelenograd, Russia) and
 274 ZNTC (Zelenograd, Russia), respectively. The detector material is high-resistivity silicon wafers with diameters of
 275 4" and 6", produced by the Float Zone method ($\rho > 5 \text{ k}\Omega \times \text{cm}$). Each side, p^+ and n^+ , contain 640 strips. The strip
 276 spacing is 95 and $103 \mu\text{m}$, respectively, and the relative angle between the strips on the two sides is 2.5° . The detectors

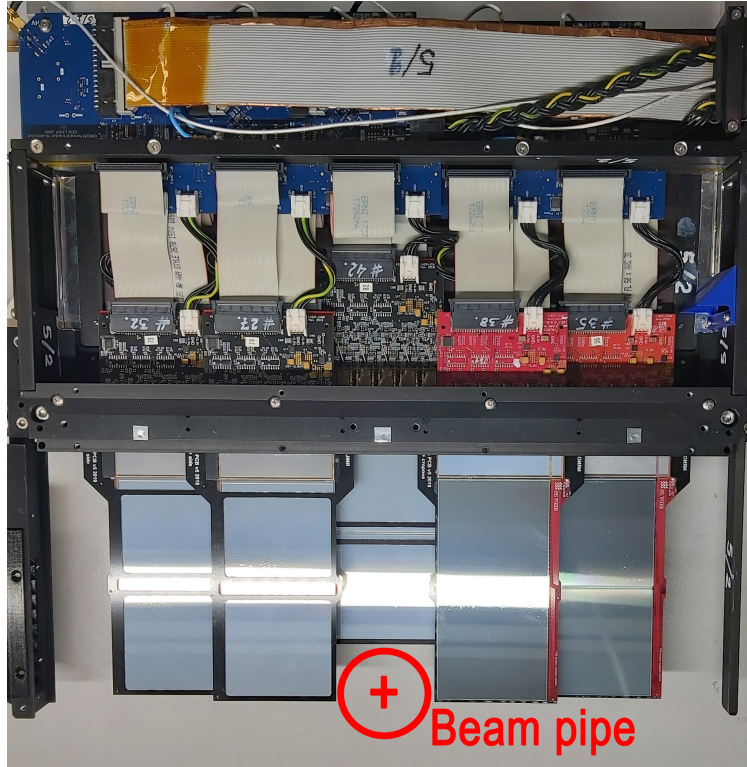


Fig. 13. The top half of the 2nd plane of the FSD. The photo is taken with removed light and electromagnetic shield in order to show the arrangement of the silicon modules and electronic boards.

277 are positioned in such a way that the strips of the p^+ side are aligned with the Y axis.

278 Fig. 14 shows a module with two DSSDs and a demonstration of US-bonding. A diagram of the FEE is presented
 279 in Fig. 15. The detector topology (DC) does not contain integrated bias resistors and capacitors for DC decoupling of
 280 the strips from the inputs of the readout electronics. The role of the RC-bias element in the DC circuit is performed
 281 by the integrated Pitch-Adapter (PA), which also performs the matching of the strip pitch with the pad topology of
 282 inputs in the FEE ASIC. Also manufactured at ZNTC, the PAs were made on the basis of Silicon on Sapphire structure.
 283 Each PA has 640 RC channels with $1\text{ M}\Omega$ polysilicon bias resistors and $120\text{ pF}/100\text{ V}$ integral capacitors. The PA-640
 284 integrated circuits have low leakage currents (less than $10\text{ pA}/\text{capacitor}/100\text{ V}$) and an electrical breakdown value of
 285 150 V , which corresponds to an electric field strength in the capacitor of more than $3\text{ MV}/\text{cm}$.

286 After passing the PA, the signals from the p^+ and n^+ strips of the detector are fed to the inputs of a 128-channel
 287 specialized integrated circuit VATAGP7.2 (IDEAS, Norway). Each electronic registration channel has a charging
 288 amplifier ($\sigma - 200\text{ e}$), a pulse shaper (peaking time $t_s = 500\text{ ns}$), and a memory capacitor which stores the pulse
 289 amplitude at trigger time. The ASIC also uses an analog multiplexer channeling 128 inputs into 1 output sent to the
 290 readout in the DAQ by ADC. Two printed circuit boards are used in each FSD module in order to accommodate its
 291 input signals, one for the 640 negative polarity signals from the n^+ strips, the other for the 640 positive polarity signals
 292 from the p^+ strips. Correspondingly, 5 ASICs are mounted on each PCB, bonding into the pitch adapters and sealed
 293 with a compound.

294 After the assembly of the modules into a half-plane, the position and rotation angles of every DSSD with respect
 295 to geodetic markers on the half-plane housing is measured using the NORGAV NVM II-5040D video meter with an
 296 accuracy of $\pm 5\text{ }\mu\text{m}$. The markers are subsequently used during the installation in order to bind the position of each
 297 detector to the common coordinate system of the experimental setup.

298 Fig. 16 illustrates the distribution of hits in the 3rd plane of the FSD observed in tests with cosmic rays and in
 299 the 2023 Xe run. Dark bands in the distribution indicate insensitive groups of 128 channels (1 chip). The number of

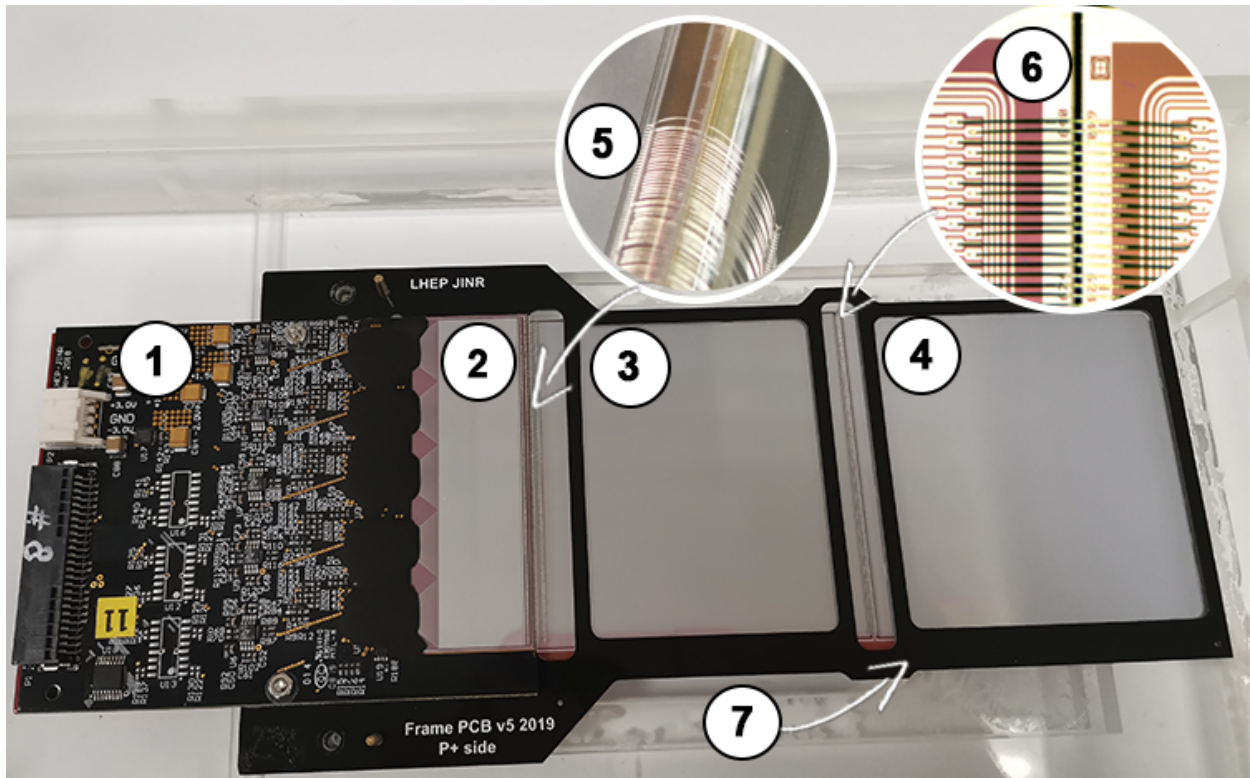


Fig. 14. Example of the FSD module. 1) Readout electronics. 2) Pitch Adapter. 3) DSSD1. 4) DSSD2. 5) Example of US-bonding PA + DSSD1. 6) Example of US-bonding DSSD1 + DSSD2. 7) Positioning frame.

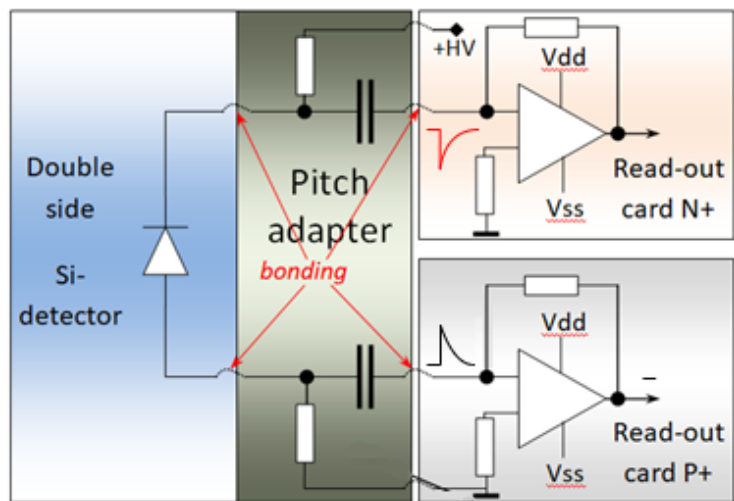


Fig. 15. Functional diagram of the signal readout from a silicon detector module.

300 such faulty chips at the end of the run was equal to 0, 1, 1, 8 for the 1st, 2nd, 3rd and 4th planes, respectively, which
 301 corresponds to 0, 1.0, 0.7 and 4.4 % of the channels. This malfunction can be due to the following reasons: 1) broken
 302 electrical contact in the transmission circuit from the chip (FEE buffer, cross-board connector, patch panel cable, long
 303 ADC-64 cable) 2) failure of the chip (no programming of the operating mode) or breakage of the US-bonding. Defects
 304 of the first type can be repaired, while the failures in the second group are of a permanent nature.

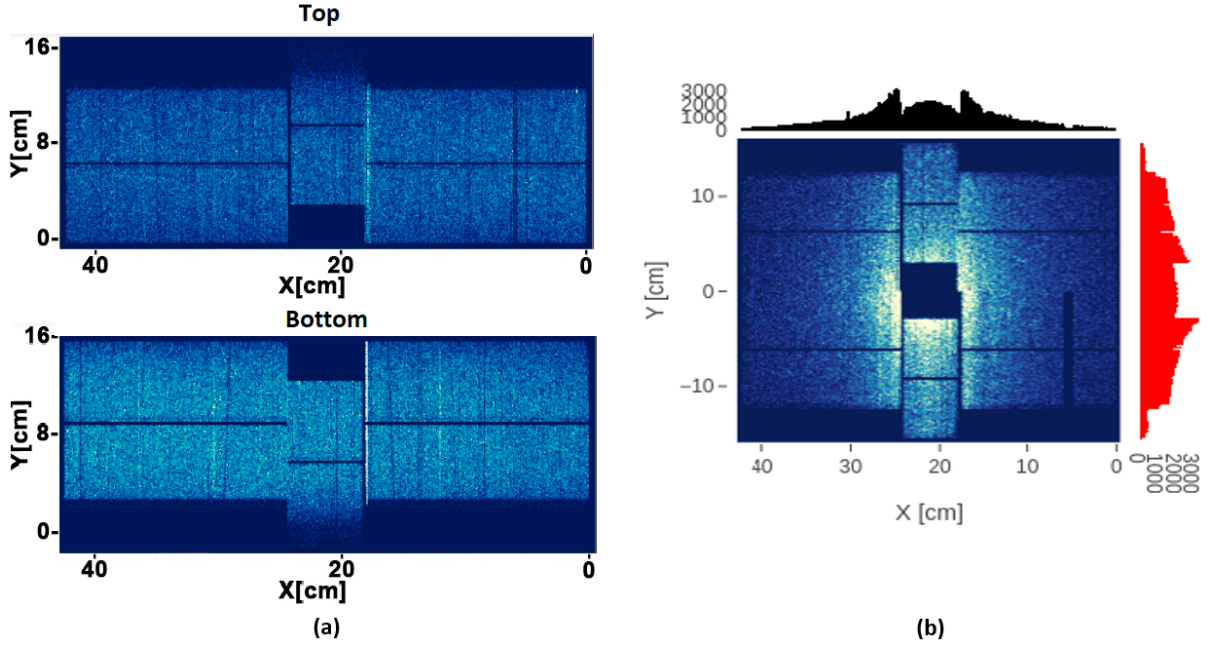


Fig. 16. *XY* distribution of hits in the 3rd plane of the FSD. (a) In tests with cosmic rays. (b) In the 2023 Xe run.

305 5.2. GEM detectors

306 Triple-GEM detectors are located inside the SP-41 analyzing magnet downstream the FSD. Full configuration of
 307 the GEM tracking system implemented in the 2023 Xe run consists of 14 detectors forming 7 tracking planes: 7 top
 308 detectors above the vacuum beam pipe and 7 bottom detectors below the pipe. Since the beam line inside the SP-41
 309 is closer to the bottom pole of the magnet, in order to cover the maximum possible acceptance, the top and bottom
 310 detectors have been designed with different active area sizes, $163 \times 45 \text{ cm}^2$ and $163 \times 39 \text{ cm}^2$, respectively.

311 5.2.1. Design of GEM detectors

312 The BM@N GEM detectors were produced using non-glue “foil-stretching” technology and assembled at CERN
 313 in the PH Detector Technologies and Micro-Pattern Technologies workshop. All three GEM foils in a detector are
 314 identical and made of a $50 \mu\text{m}$ thick Kapton foil covered on both sides with $5 \mu\text{m}$ copper electrodes. The foils are
 315 perforated by holes of about $70 \mu\text{m}$ diameter, separated by a distance of $140 \mu\text{m}$. The gaps between the electrodes are
 316 shown in Fig. 17 (a).

317 The anode plane is used for the readout and organized as a multilayered board with two types of parallel strips:
 318 aligned with the vertical axis and inclined by 15 degrees with respect to it, as shown in Fig. 17 (right). The width of
 319 vertical and inclined strips is $680 \mu\text{m}$ and $160 \mu\text{m}$ respectively, while the pitch for both types of strips is $800 \mu\text{m}$. The
 320 readout plane is subdivided by two halves and, in addition, a separate readout is organized for the region close to the
 321 beam pipe where higher density of hits is expected. The size of this “hot zone” is approximately $80 \times 15 \text{ cm}^2$. The
 322 readout FEE boards are mounted on the frames of the detectors outside of the acceptance. More details on the design,
 323 tests and preparation of the detectors can be found in [17, 18].

324 The main parameters of the GEM system are presented in Table 4.

Table 4. Main parameters of the GEM system.

	Top GEM detector				Bottom GEM detector			
	Left readout board		Right readout board		Left readout board		Right readout board	
	Outer zone	Hot zone	Outer zone	Hot zone	Outer zone	Hot zone	Outer zone	Hot zone
Number of X strips	1019	500	1019	500	1021	501	1019	500
Number of Y strips	1081	488	1130	506	1062	488	1111	506
Total number of detector strips	6243				6208			
Detector active area, cm^2	163×45				163×39			
FEE on one detector	50				50			
Number of detectors	7				7			
Total active area, m^2	9.58							
Total number of FEE channels	87157							

5.2.2. Mechanical support

The mechanical support of the GEM detectors inside the SP-41 magnet was designed and manufactured by LLC “Pelcom Dubna Machine-Building Plant”, Russia. The support structure is made of non-magnetic material and satisfies strict requirements for precise positioning of the detectors. The weight of one GEM detector equipped with mechanics, front-end electronics and cables is about 19.5 kg. The whole assembly of 14 GEM detectors can be vertically adjusted by ± 10 mm relative to the surface of the magnet coil. In addition, the setup allows shifting each GEM detector vertically by ± 5 mm with respect to the mechanical support. The accuracy of positioning of each detector relative to the other (one half-plane relative to the other half-plane) does not exceed 0.2 mm. After the installation and alignment of each detector, the coordinates of the frame corners and the center of the semi-circular notch for the beam pipe are measured with an accuracy better than 0.5 mm.

The detector installation sequence is as follows: 1) the bottom detectors are installed sequentially, starting from the detector closest to the target; 2) the carbon beam pipe is installed on top of the bottom detectors; 3) the top detectors are installed sequentially, starting from the detector closest to the target. A photo of the installation process is shown in Fig. 18.

Prior to the installation a detectors were tested with cosmic muons in order to determine the gain uniformity across the detector area. A lower amplification in the outer parts of the detectors was observed, with typical variations in the range ± 20 %. The detectors, which, due to this effect, can have lower efficiency in the outer parts, were installed closer to the target, where outer regions are less significant for track reconstruction.

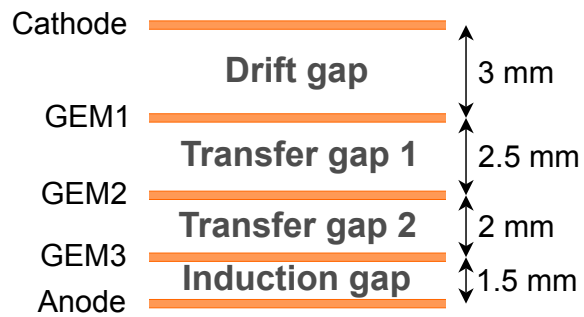
5.2.3. Gas system

The $Ar(80)C_4H_{10}(20)$ gas mixture was chosen for the operation in the 2023 Xe run, while the overall GEM detector amplification was maintained at the level of 3×10^4 . The H_2O and O_2 removal filter was installed in the gas system after the gas mixer. The gas line was divided into two identical lines for independent connection of the top and bottom GEM detectors. Two rotameters were installed in the lines, allowing one to regulate the gas flow. Each line connected a group of top or bottom detectors in series, starting with the detector closest to the target. The small GEM detector (see the section “Beam and trigger detectors”) was connected last in the line for the bottom detectors. The gas flow rate in each line during the 2023 Xe run was at the level of 3 l/h.

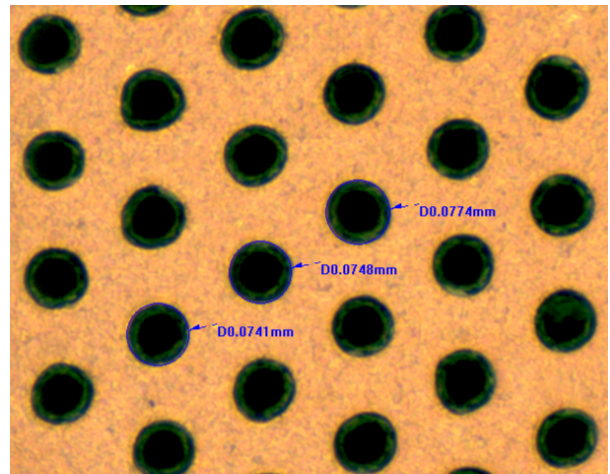
5.2.4. Front-end electronics

Front-end electronics is based on the 32-channel integrated circuit VA163 (IDEAS, Norway). Each channel of the ASIC has a charge sensitive preamplifier, a shaper with $2 \mu s$ peaking time, and a sample holder circuit. An analog multiplexer sends channel by channel 32 sampled signals into one serial readout. Four ASICs are joined in one front-

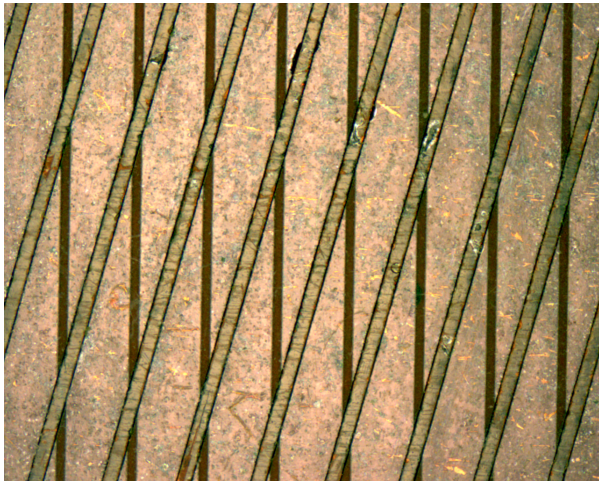
³⁵⁵ end board. The multiplexed data from each board are transmitted through 13 *m* of twisted pair flat cable to the 12-bit
³⁵⁶ analog-to-digital converter. A more detailed description of the FEE can be found in [\[19\]](#).



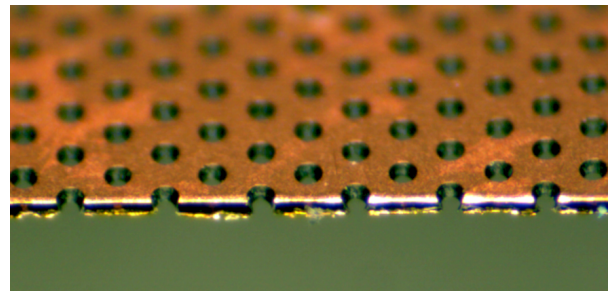
a)



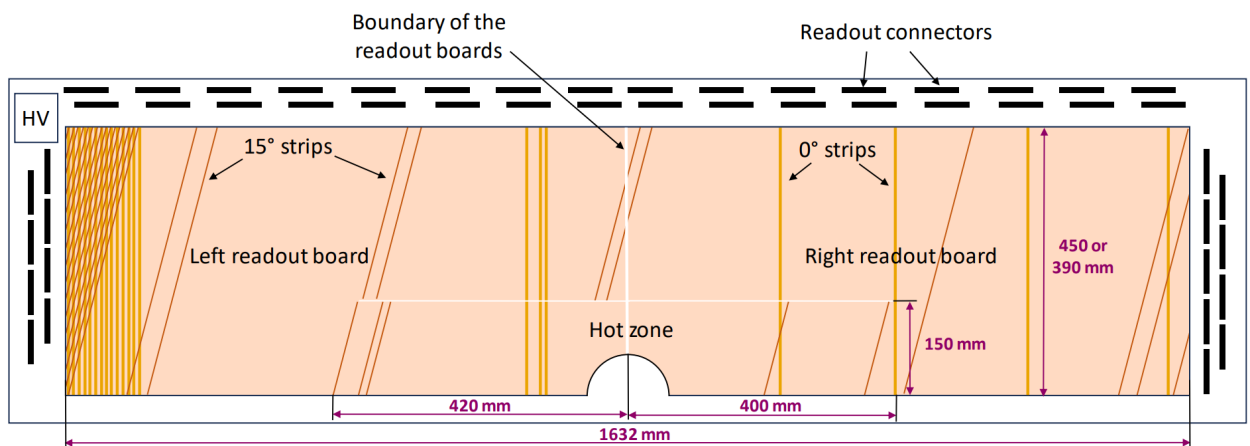
b)



c)



d)



e)

Fig. 17. Design of the GEM detectors. (a) Cross-section of the triple GEM detector. (b) Schematic view of the detector readout board.

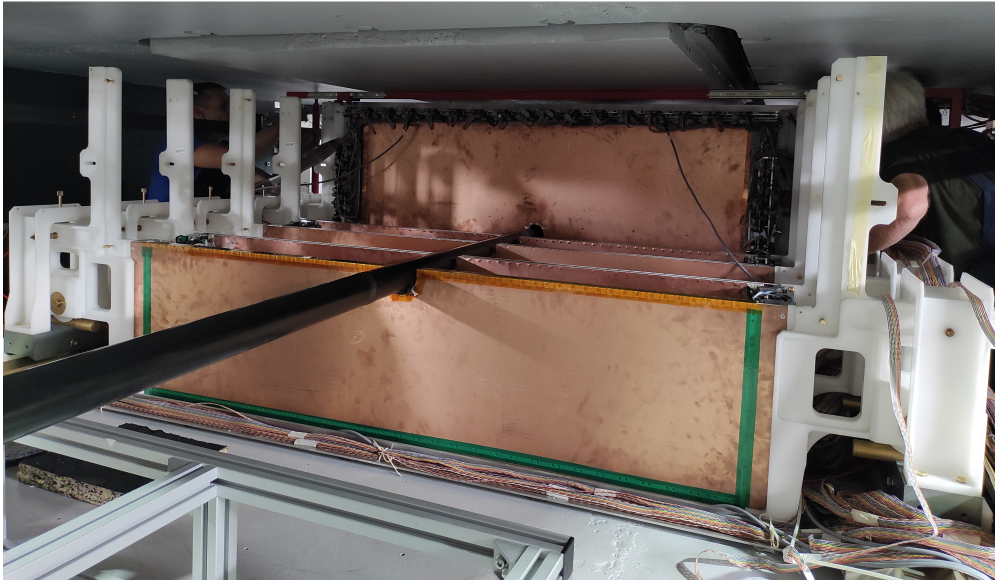


Fig. 18. Photo of GEM detectors installation viewed from the back side of the SP-41 magnet (in the direction opposite to the beam).

6. TOF systems

Two time-of-flight systems are used in BM@N for charged particle identification. The first system, TOF400, is placed at about 4 meters from the target and consists of two arms to the left and right of the beam axis. It is focused on identifying particles flying at high polar angles. The time-of-flight distance does not allow effective separation of charged particles near the beam axis. The second wall, TOF700, is located at a distance of about 7 meters from the target, sufficient for an effective separation of particles at small angles. The arrangement of both systems provides continuous geometric acceptance and overlap with the FSD, GEM and Outer Tracker subsystems. The choice of detectors and their parameters was dictated by the following requirements:

- high granularity and rate capability to keep the overall system occupancy below 15 %, while minimizing efficiency degradation due to double hits;
- position resolution better than 1 cm in order to provide effective matching of TOF hits with tracks;
- high combined geometrical and detection efficiency (better than 85 %);
- separation of pions and kaons in the momentum range $0.1 < p < 3 \text{ GeV}/c$;
- separation of kaons and protons in the momentum range $0.3 < p < 5 \text{ GeV}/c$.

To achieve necessary performance, a strip-readable Multigap Resistive Plate Chamber (MRPC) detector was chosen for both TOF subsystems. This type of detectors is widely used for time-of-flight measurements. It shows good efficiency, excellent time resolution and the ability to work with particle flux up to tens of kHz/cm^2 .

6.1. TOF400

The left and right arms of the TOF400 system are placed symmetrically with respect to the beam. Each arm consists of two gas boxes (modules), each having 5 MRPC detectors (Fig. 19). The active area of one detector is $60 \times 30 \text{ cm}^2$. Inside the box, the active areas of adjacent detectors overlap vertically by 50 mm , while the horizontal overlap of the gas boxes ensures crossing of the detector active area by 50 mm as well. This makes the total active area of each of the two arms to be equal to $1.10 \times 1.3 \text{ m}^2$, matching the geometrical acceptance of the $1 \times 1 \text{ m}^2$ CSCs and covering a significant fraction of the GEM system acceptance. Each gas box is formed by an aluminum frame closed from the front and back sides by aluminum honeycomb plates, which provide sufficient rigidity while having small thickness in radiation lengths.

Fig. 20 shows a schematic cross-section of the TOF400 MRPC. The detector consists of three stacks inserted between two outer 1.5 mm thick PCBs and separated by two inner PCBs, also 1.5 mm thick. In order to add stiffness to the structure, fiberglass honeycombs with a thickness of 10 mm were glued on the outer sides of the external PCBs. Each stack has 5 gas gaps between glass sheets, which are used as resistive electrodes. The two external glass sheets in a stack have a thickness of $400 \mu\text{m}$, while the four internal sheets are $280 \mu\text{m}$ thick. Fishing line as a spacer defines the $200 \mu\text{m}$ gap between all the glass plates. High voltage is applied to the outer part of the external glass electrodes covered by conductive paint with surface resistivity of about $2 - 10 \text{ M}\Omega/\text{sq}$. All internal glass electrodes are left electrically floating. Two PCBs with pickup readout pads are placed on both sides of the inner stack, one serving as the cathode readout plane, the other as the anode one. Correspondingly, the HV is applied in an alternating sequence, as shown on the right side of Fig. 20, in order to form a symmetrical configuration for the cathode and anode readout planes. Such a configuration was chosen to ensure that propagation of signals to the FEE has equal speed on positive and negative lines, thus preventing dispersion of the differential signal.

Readout pads are strips of $300 \times 10 \text{ mm}^2$ arranged vertically with a 12.5 mm pitch, making 48 readout strips in each PCBs. A 2.5 mm spacing between adjacent strips is introduced in order to reduce crosstalk between them. Signals from the strips are transferred to the front-end electronics by twisted pair cables. In order to obtain a better time resolution and determination of hit coordinate along the strip, the signals are read out from both ends of the strip.

The FEE of the TOF400 is based on the NINO amplifier/discriminator ASIC developed at CERN for the time-of-flight system of the ALICE experiment [20]. The chip is processed on $0.25 \mu\text{m}$ technology and has 8 input channels. Each channel includes an ultra-fast preamplifier with peaking time less than 1 ns , a discriminator with a minimum detection threshold of 10 fC , and an output stage which provides an LVDS output signal. The duration of the LVDS signal is proportional to the charge of the input signal and can be used for the amplitude-time correction. The 24-channel FEE board, which combines signal processing for three NINO chips, was developed at LHEP JINR [21]. In order to ensure optimal operation of the FEE, the boards are placed as close to the MRPC as possible and mounted on

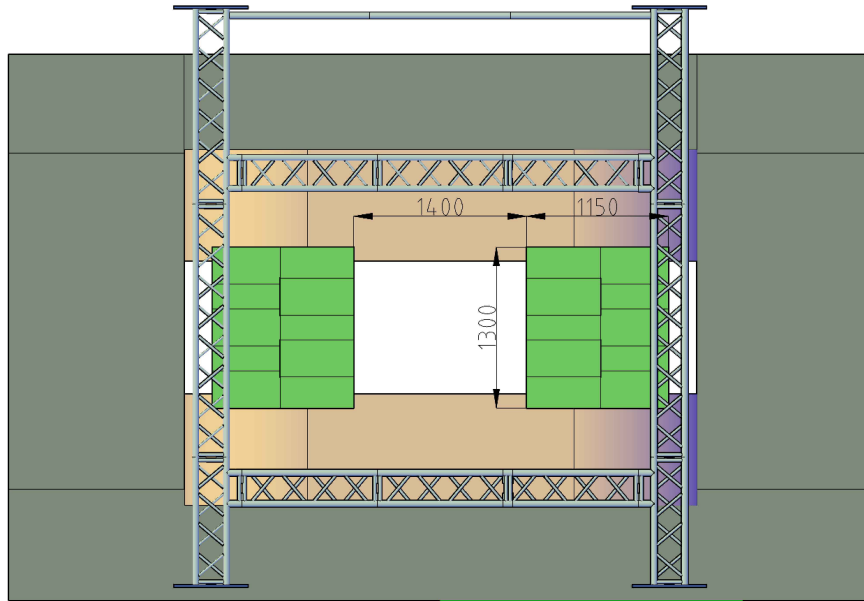


Fig. 19. Schematic view of the TOF400 system.

406 the front cover of the gas box. Measurements with a test signal from a generator showed an intrinsic time resolution of
 407 the FEE chain of about 7 ps . Additional features of the FEE board include the ability to remotely control the threshold
 408 levels of the NINO discriminators and to measure the supply voltage and temperature on the board via the RS-485
 409 interface.

410 LVDS signals from the FEE boards are transmitted over a distance of up to 10 m via a special cable without loss of
 411 time resolution. The signals are digitized in 72-channel time-to-digital converters (TDC72VHL) based on the HPTDC
 412 chip [23]. The TDC72VHL were developed at LHEP JINR and operate in ultra high resolution mode with a binning
 413 of 23.4 ps . Such fine binning allows determining the leading and trailing edges of the input LVDS signals with high
 414 accuracy. The TDCs exhibit significant integral non-linearity, which, if not corrected, causes significant degradation

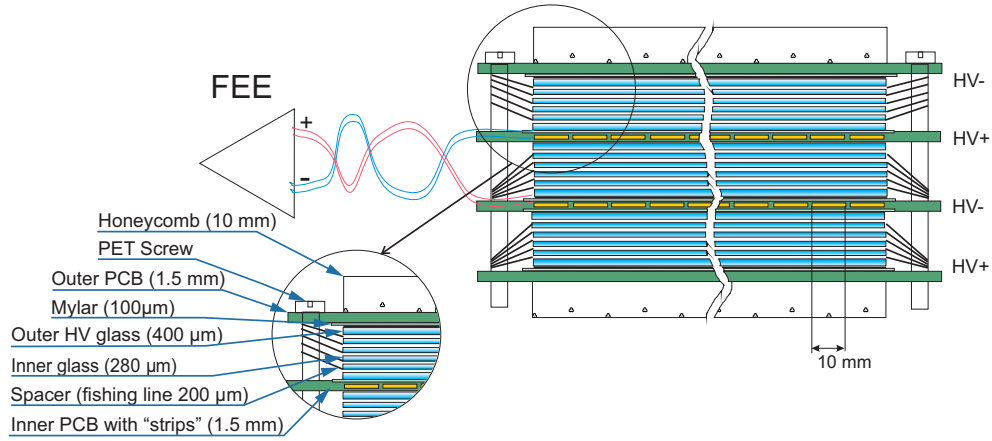


Fig. 20. Schematic cross-section of the TOF400 MRPC.

415 of the time resolution. The method of uniform filling the TDC time window with random events (code density test)
 416 is used for non-linearity calibration of every channel of the TDC module. After applying the non-linearity correction,
 417 the intrinsic time resolution of individual TDC72VHL channels is equal to 20 ps on average.

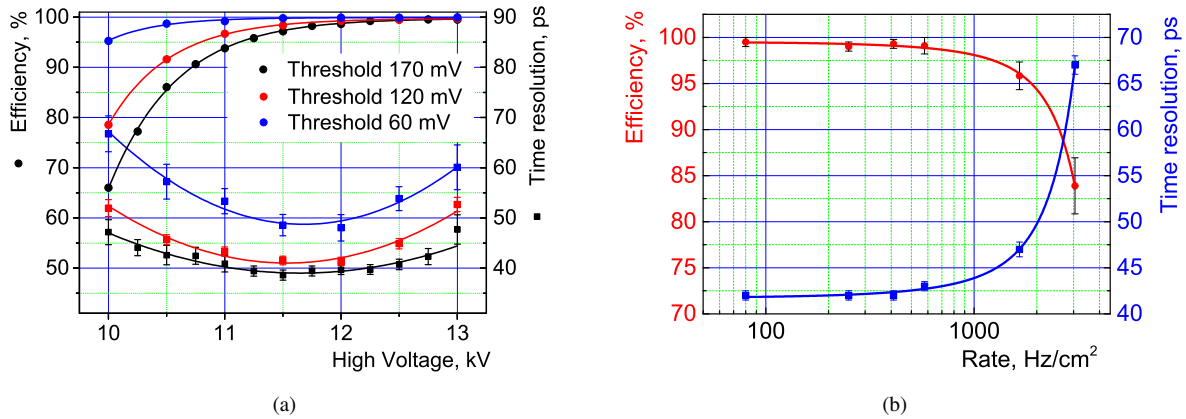


Fig. 21. Performance of a TOF400 MRPC detector. a) The detector efficiency and time resolution as a function of applied HV for different NINO thresholds. b) The dependence of the detector performance on the particle flux for 11.5 kV HV and 120 mV threshold.

418 A full scale MRPC prototype with a complete readout chain and a 90% $C_2H_2F_4$ + 5% $i-C_4H_{10}$ + 5% SF_6 gas
 419 mixture was tested in the Nuclotron deuteron beam [24]. A fast Cherenkov counter with a time resolution of 37 ps
 420 was used as a start detector. The measured efficiency and time resolution as a function of high voltage for different
 421 levels of the NINO discriminator threshold are presented in Fig. 21a. All the results include contributions from the
 422 front-end and data acquisition electronics. Based on the measured prototype performance, a high voltage of 11.5 kV
 423 and a discriminator threshold of 120 mV were chosen as the operating point of the TOF400 modules. With these
 424 settings, the dependence of efficiency and time resolution on the particle rate was studied with the prototype. The
 425 results of these tests are presented in Fig. 21b. Monte Carlo simulations show that under the BM@N conditions, even
 426 at the highest heavy ion beam intensity, the particle flux in the TOF400 does not exceed 1 kHz/cm². Therefore, time
 427 resolution better than 50 ps and efficiency higher than 95% are expected.

428 6.2. TOF700

429 The TOF700 wall is placed at about 7 meters from the target and has an active $X - Y$ area of $3.2 \times 2.2 m^2$ defined
 430 to overlap with the geometrical acceptance of the Outer Tracker detectors (CSC $2.2 \times 1.5 m^2$) as well as to provide
 431 substantial overlap with the GEM system acceptance. At the center of the TOF700 wall, there is an opening for
 432 the vacuum beam pipe. Since the hit density of hits from particles produced in heavy ion collisions is significantly
 433 higher in the region close to the beam, two types of MRPC detectors are used for the TOF700: “cold” – with an
 434 active area of $30.3 \times 56 cm^2$ and 16 readout strips of $18 \times 560 mm^2$ for the outer area with a low particle flux, and
 435 “warm” – with an active area of $16 \times 35.1 cm^2$ and 32 strips of $10 \times 160 mm^2$ for the area near the beam line. The
 436 horizontal orientation and size of the readout strips were dictated by the expected hit occupancy and the requirement
 437 of unambiguous matching of hits with particle tracks. The arrangement of the TOF700 MRPCs in the XY plane is
 438 shown in Fig. 22. The detectors are mounted on two sub-walls, which can slide relative to each other to facilitate
 439 access for installation and maintenance of the detectors. In addition, the MRPCs in each sub-wall are arranged in two
 440 layers in order to provide geometrical overlap between adjacent detectors.

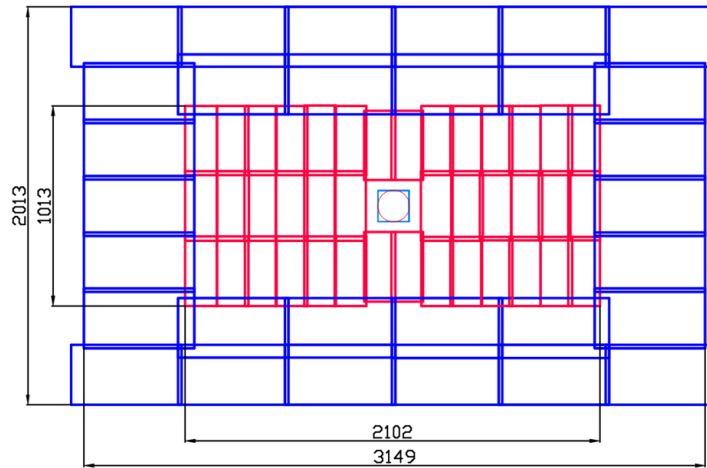


Fig. 22. Arrangement of 40 “warm” (red) and 32 “cold” (blue) MRPCs in the TOF700 active area.

441 “Cold” and “warm” MRPCs have similar two-stack design with a single anode readout plane placed between the
 442 stacks. A schematic cross-section of a “cold” MRPC is shown in Fig. 23. Each stack is formed by six $0.67 mm$ thick
 443 glass plates with bulk resistivity of $2 \times 10^{12} \Omega \times cm$. Fishing line spacers define a $0.3 mm$ gap between the glass sheets.
 444 Graphite conductive coating with surface resistivity of $\sim 1 M\Omega/sq$ is painted on the outer surfaces of the external
 445 glass plates in order to apply both high voltage and ground connections. The anode readout plane is arranged on a
 446 $100 \mu m$ one-sided PCB. Unipolar signals are taken from both ends of the strips, which makes it possible to determine
 447 the coordinate of the particle hit along the strip by measuring the time difference between the signals. Each detector is
 448 placed in an individual gas box, which is formed by a $2.5 mm$ thick aluminum frame and two cover plates. One cover
 449 is made of $2.5 mm$ thick PCB and is designed to take out signal wires from the box volume to the readout electronics.
 450 The other cover is made of $1.5 mm$ thick aluminum sheet.

451 The design of “warm” MRPCs has only minor modifications. In order to increase their rate capability, the gas
 452 gaps and thickness of the glass plates in warm MRPCs are reduced to $0.22 mm$ and $0.55 mm$, respectively. Such a
 453 reduction leads to lower signal amplitudes due to increased anode strip – cathode capacity. To compensate for this
 454 signal weakening, the number of gaps in the chamber was increased from 10 to 12 (six gaps per stack).

455 The FEE boards are developed specially for BM@N. Signals from the MRPC are sent to the FEE over 50Ω
 456 coaxial cables with MMCX connectors. The boards are based on the NINO ASICs, which, as already mentioned,
 457 process the signals in such a way that the duration of the LVDS output signals is proportional to the amplitude of the

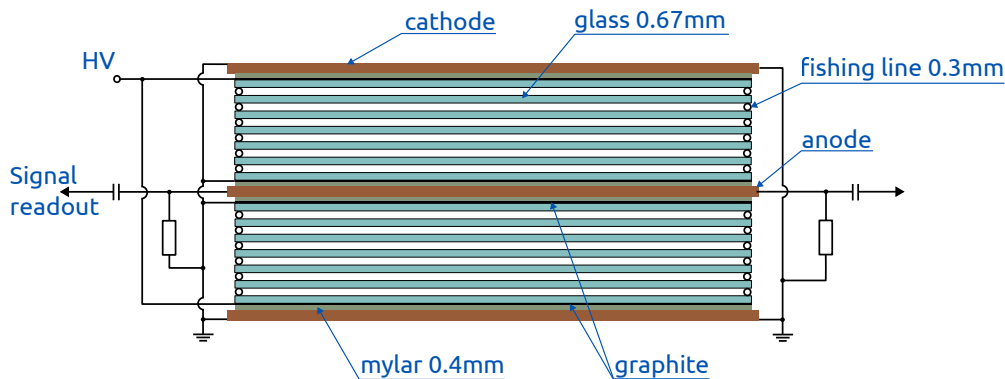


Fig. 23. Schematic view of the MRPC detector for the TOF700 system.

458 input signals, suitable for implementation of the time-over-threshold method. The output signals are transmitted to
 459 the digitizing module using DHR-78F connectors. A 64-channel VME TDC64VHLE time-to-digital converter based
 460 on the HPTDC chip is used for digitization. With a special module (PWR&CTRL) it is possible to remotely control
 461 the power supply, the discrimination threshold and hysteresis value in the FEE boards.

462 Prototypes of the “cold” and “warm” TOF700 detectors were tested in the secondary muon beam of the U-70
 463 accelerator at IHEP (Protvino, Russia). The test was carried out at the “MUON” facility with a particle flux of about
 464 $1 \text{ kHz}/\text{cm}^2$ ([22]). The test results of both prototypes are shown in Fig. 24. The time resolution of the MRPCs with a
 465 complete chain of electronics (FEE and readout) is at the level of 60 ps. The efficiency is more than 95

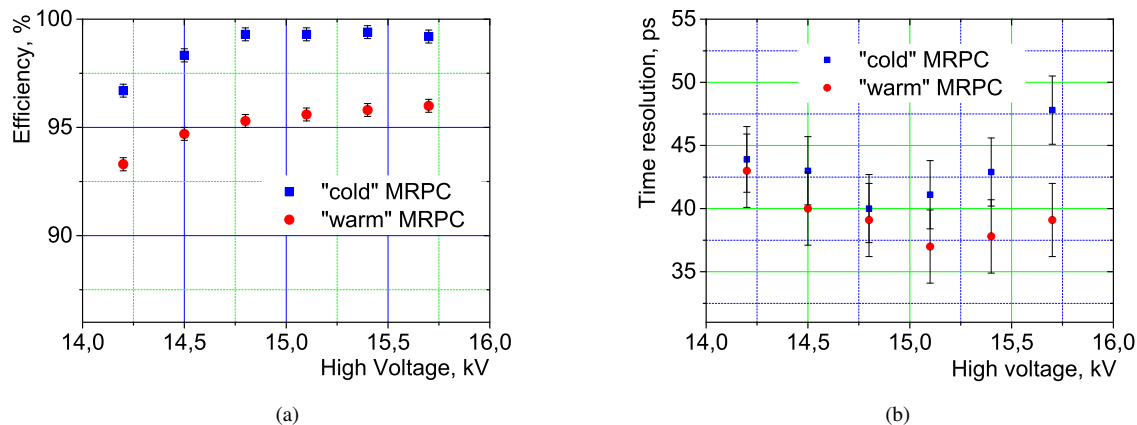


Fig. 24. Performance of MRPCs designed for the TOF700 system. a) Detector efficiency. b) Time resolution.

466 Both TOF400 and TOF700 systems use the same non-flammable Freon rich gas mixture containing 90 % $C_2H_2F_4$,
 467 5 % $i-C_4H_{10}$, and 5 % SF_6 . A simple open-loop gas system was designed for the BM@N experiment. This system is
 468 based on the MKS 1479A controllers for measuring and adjusting the absolute flow of components with an accuracy
 469 of 0.3 %. The flow rate of the gas mixture can be adjusted in the range from 6 l/h to 90 l/h. The typical operational
 470 flow is 21 l/h which corresponds to of 2 volumes exchange per day. Also, one additional channel is available to purge
 471 the system with nitrogen for cleaning and drying. A special PC program has been written to control the parameters of
 472 the gas system via the Ethernet interface.

473 The MRPC detector operates at very high voltages of 12 kV and 15 kV for the TOF400 and TOF700, respectively.
 474 On the other hand, the dark currents of the detector are quite small at the level of tens of nA. Also, the detector is very
 475 sensitive to voltage ripples due to the large capacitive coupling between the high voltage layer and the readout strips.

476 Therefore, the high voltage system is subject to high requirements for voltage stability and current measurement
 477 accuracy. The high voltage power supply systems for both TOF subsystems are based on commercially available
 478 Iseg modules (Iseg Spezialelektronik GmbH, Germany) and a system module specially designed by “HVSys” (JINR,
 479 Dubna, Russia). Remote control of all elements of the system is organized via Ethernet interface.

480 The main parameters of the TOF400 and TOF700 subsystems are summarized in Table 5.

Table 5. Main parameters of TOF system.

	TOF400	TOF700
MRPC active area	$30 \times 60 \text{ cm}^2$	$30.3 \times 56 \text{ cm}^2$ “cold” $16 \times 35.1 \text{ cm}^2$ “warm”
FEE on one MRPC	96	32 for “cold” 64 for “warm”
Number of MRPC	20	30 “cold” 40 “warm”
Total active area	$2 \text{ Arms} \times 1.1 \times 1.3 \text{ m}^2$	$3.2 \times 2.2 \text{ m}^2$
Total number of FEE channels	1920	3520

481 **7. Outer Tracker**

482 The detectors of the Outer Tracker are situated downstream of the analyzing magnet. In the 2023 Xe run the
483 Outer Tracker consisted of two large aperture drift chambers (DCH) and five cathode strip chambers (CSC), four
484 of them $1.1 \times 1.1 m^2$ (small) and one $2 \times 1.5 m^2$ (large). Track localization in the Outer Tracker is used not only
485 to improve particle momentum reconstruction, but also to facilitate matching of tracks reconstructed in the Central
486 Tracking System with corresponding hits in the time-of-flight detectors. Therefore, the size and location of the small
487 CSC were chosen to provide significant overlap with the TOF400 acceptance, while the DCH were placed to cover
488 most of the TOF700 acceptance. The granularity of the DCH is sufficient to perform measurements with beams of
489 light and medium nuclei. However, in experiments with Au or Bi beams, the DCH occupancy becomes too high to
490 perform efficient track separation. Therefore, in the process of preparation for the experiments with heaviest ions, the
491 two drift chambers will be replaced by two large cathode strip chambers. The first of them was tested during the 2023
492 Xe run. In the final configuration, relative position of the TOF700 and two large CSC will be optimized.

493 *7.1. Drift chambers*

494 The drift chambers, formerly used in the NA48 experiment at CERN [25], have an octagonal shape with a trans-
495 verse width of $2.9 m$ (Fig. 25). Their fiducial area is about $4.5 m^2$, the hole for the beam pipe in the center of the
496 chamber has a diameter of $160 mm$. The chambers are constructed with minimal amount of material along the beam
497 direction, thus reducing multiple scattering effects.

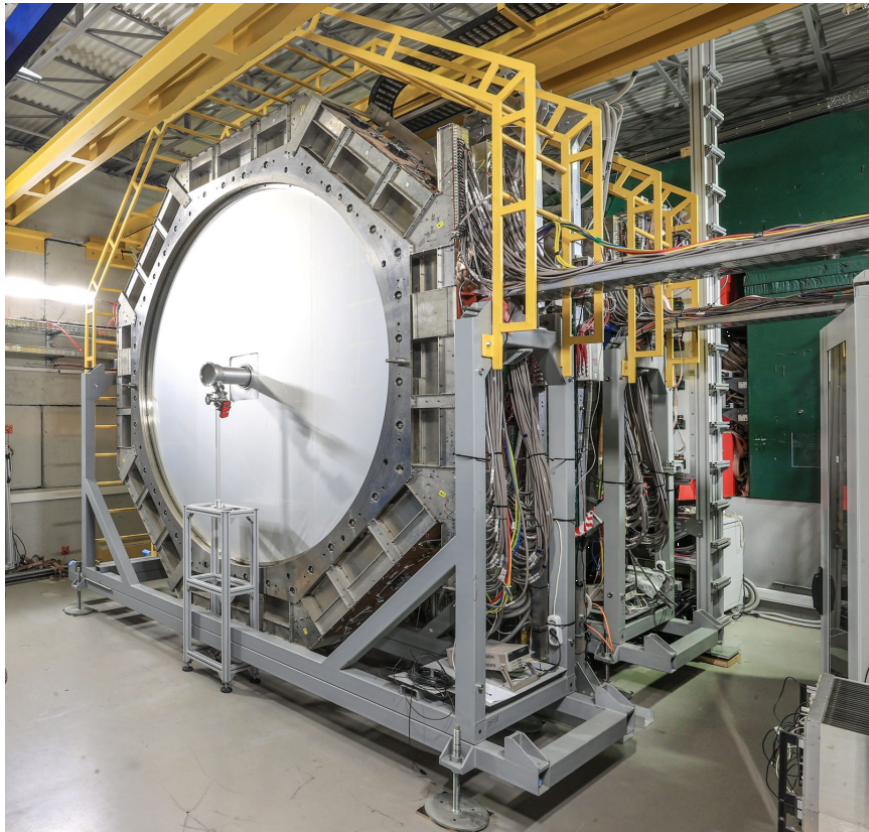


Fig. 25. DCH integrated into the BM@N experimental setup.

498 Each chamber contains four X, Y, U, V coordinate planes with wire inclination angles with respect to the Y axis of
499 $0^\circ, 90^\circ, -45^\circ$ and $+45^\circ$, respectively.

500 A schematic view of the drift cell geometry is shown in Fig. 26. In order to resolve left-right ambiguity of the hit
 501 position relative to the signal wire, every coordinate plane has two staggered rows of wires. Each coordinate plane
 502 has 2×256 signal wires with a wire pitch of 10 mm . The central wires in the region of the beam pipe are split in two.
 503 The sense wires are grounded. The electric field is created by the negative voltage applied to two planes of field
 504 wires located on each side of the sense wire plane at a distance of 3 mm .

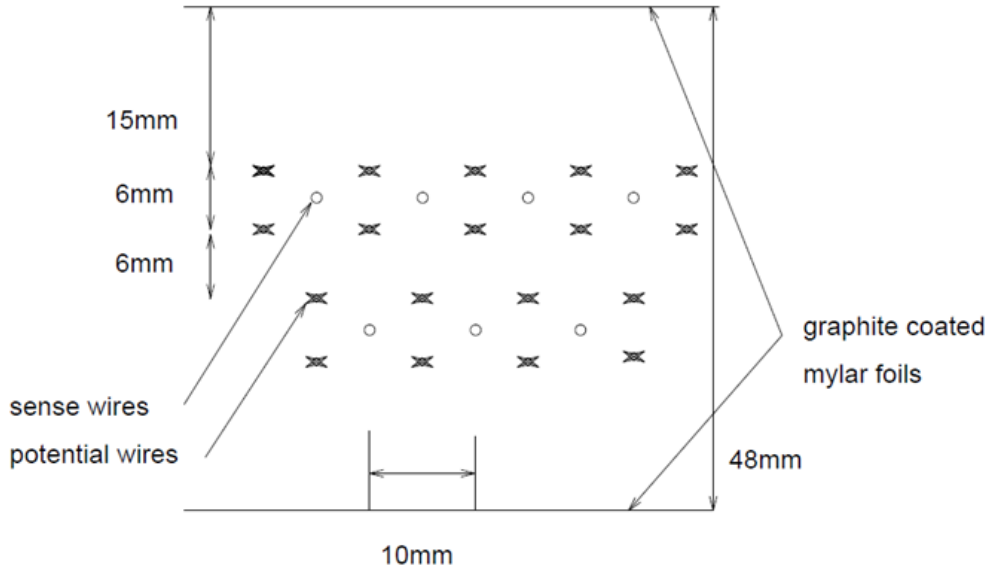


Fig. 26. Drift cell geometry of the DCH.

505 The sense wires made of gold-plated tungsten have a diameter of $20\ \mu\text{m}$, while the gold-plated Ti-Cu field wires
 506 have a diameter of $120\ \mu\text{m}$. Thin Mylar foils ($22\ \mu\text{m}$) coated with graphite are used to shape the electric field in the
 507 drift cell. In addition, they serve as walls separating adjacent X, Y, U, V coordinate planes.

508 The chambers normally operate at a high voltage of about $2\text{--}2.5\text{ kV}$ between the field and sense wires, whereas
 509 the Mylar foils are kept at a negative voltage of $1\text{--}1.5\text{ kV}$. Typical gas amplification for such operating conditions is at
 510 the level of 2×10^4 . A drift distance of 5 mm corresponds to a $\sim 100\text{ ns}$ drift time, which ensures high rate capability
 511 of the detector.

512 The front-end amplifiers and discriminators developed for the readout of the DCH in the NA48 experiment [26]
 513 are used in the BM@N without modifications. The FEE cards are mounted on the frame of the drift chambers. The
 514 amplifiers are designed to provide accurate timing with minimal cross-talk between neighbouring channels. For pulses
 515 with a 10 ns rise time, the cross-talk is suppressed with $\gtrsim 46\text{ dB}$. The outputs of the amplifiers are AC-coupled to
 516 high-speed discriminators in LeCroy MVL407 IC units. The discriminator thresholds are set based on an external
 517 DC voltage and can be remotely controlled. The discriminator output is a differential ECL pulse with 50 ns width
 518 followed by 50 ns of deadtime. The output pulses are transmitted via 12 m long twisted pair cables to TDC64VL
 519 VME modules, developed by AFI Electronics (Dubna, Russia). These 64-channel 100 ps multihit TDCs provide
 520 timestamp of the pulse front. The overall accuracy of the entire readout chain is about 1 ns .

521 7.2. Cathode strip chambers

522 The active area of the small CSC is $113 \times 107\text{ cm}^2$, while the large chambers have an active area of $219 \times 145\text{ cm}^2$.
 523 Both types of the CSC have similar design features. All chambers have one detection layer consisting of a plane of
 524 anode wires stretched between two cathode planes (see Figs. 27, 28). The anode wires form a horizontal grid with a
 525 step of 2.5 mm in Y . They are made of gilded tungsten and have a diameter of $30\ \mu\text{m}$. In order to reduce anode wire
 526 deflection and to reinforce the flatness of the anode plane, vertical support wires are added to the mechanical design of
 527 the chambers. The support wires are made of stainless steel, have a diameter of 0.3 mm and are insulated by a 0.8 mm
 528 thick Teflon cladding.

529 The readout of induced signals is arranged on both front and back cathode planes made of PCBs with parallel
 530 metal strips. The inclination angles of the strips with respect to the vertical axis is 0 degrees (X coordinate) in one of
 531 the cathode planes and 15 degrees (Y coordinate) in the other. The pitch of the X and Y strips is 2.5 mm.

532 Due to the large multiplicity of charged particles in heavy ion collisions, the readout layer is divided into outer
 533 (cold) and inner (hot) zones, as shown in 28. The size of the inner zone is $-14 < Y < 14$ cm and $-24 < Y < 24$ cm in
 534 the small and large chambers, respectively. Each cathode plane in the small CSC is composed of two printed circuit
 535 boards, top and bottom. The cathode planes of the large chambers are assembled of eight PCBs, four in the top half
 536 of the plane and four in the bottom one.

537 To enhance the structure rigidity the PCBs are glued on support honeycomb panels. Furthermore, in order to
 538 prevent chamber deformation, the distance between the two cathode planes is fixed by additional spacers. The distance
 539 between cathode and anode planes was a subject of optimization and varies from chamber to chamber in the range
 540 from 3.4 to 3.8 mm. A larger gap increases the number of adjacent strips with induced signal above the threshold, the
 541 width of the cluster on average spans over 6 strips, i.e. 15 mm. On the other hand, a smaller than 3.4 mm gap results
 542 in a higher probability of electric discharge. The cathode planes are grounded, and a high voltage of about +2.4 kV
 543 is applied to the anode wires.

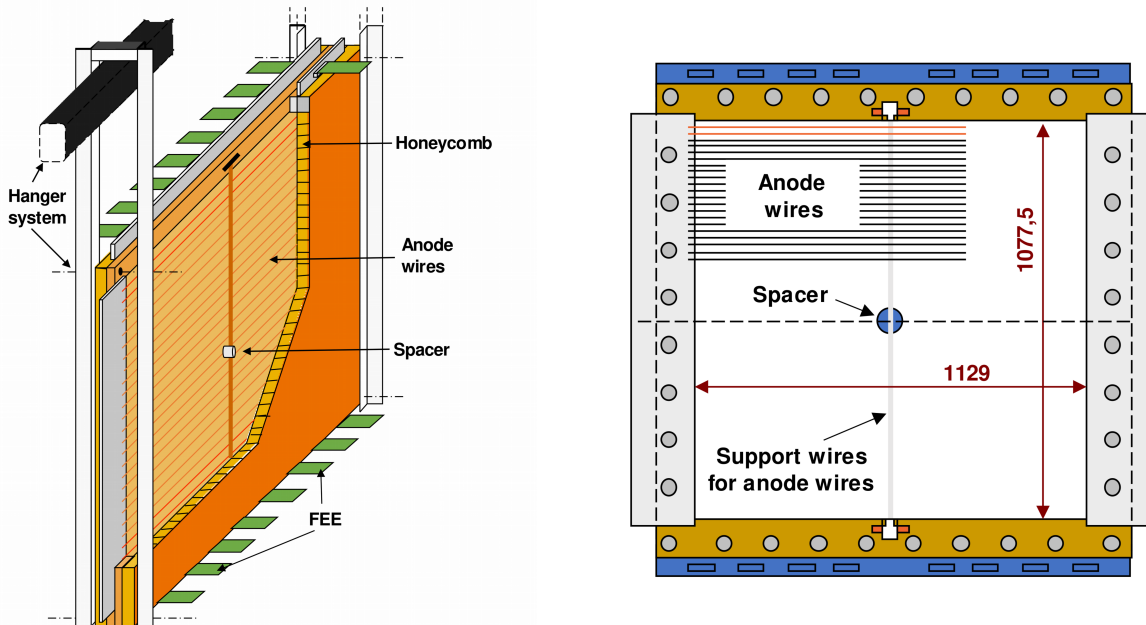


Fig. 27. Schematic view of the small CSC.

544 The CSC front-end electronics is based on the same charge sensitive preamplifier chip VA163 as used for the
 545 GEM detectors. The multiplexed data from each FEE board are transmitted through a twisted pair flat cable to 12-bit
 546 analog-to-digital converter (ADC) modules read out by the data acquisition system. The full configuration of the
 547 Outer Tracker with six CSCs will have ~ 30100 readout channels and is planned to be integrated into the BM@N
 548 experimental setup in the next physics run.

549 7.3. Gas system

550 All chambers of the Outer Tracker were operated with $Ar(75\%) + C_4H_{10}(25\%)/C_3H_8O(vapor)$ gas mixture. The
 551 gas system (Fig. 29) consists of two parts: 1) the mixer system, which delivers a mixture of gases in a required ratio
 552 and pressure to downstream elements; 2) the distribution system, which delivers the gas in well defined quantities

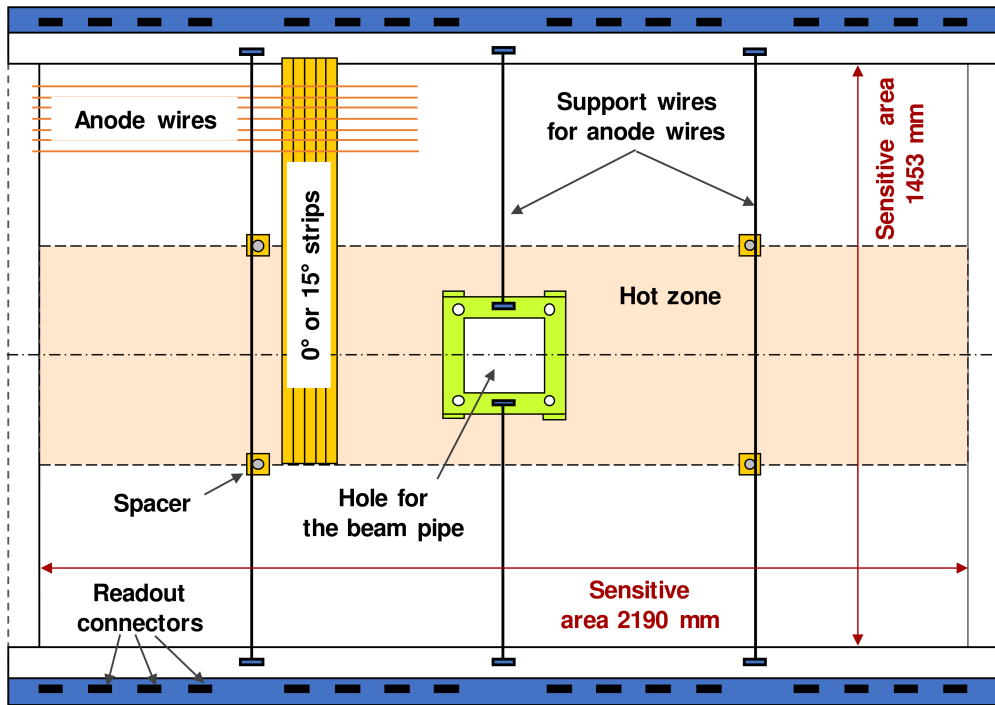


Fig. 28. Technical drawing of the large cathode strip chamber (the 15-degree strips are not shown).

553 to the individual detectors. Power supply and readout module MKS 647C and mass flow controllers used in the gas
 554 distribution system are produced by MKS Instruments, Inc.

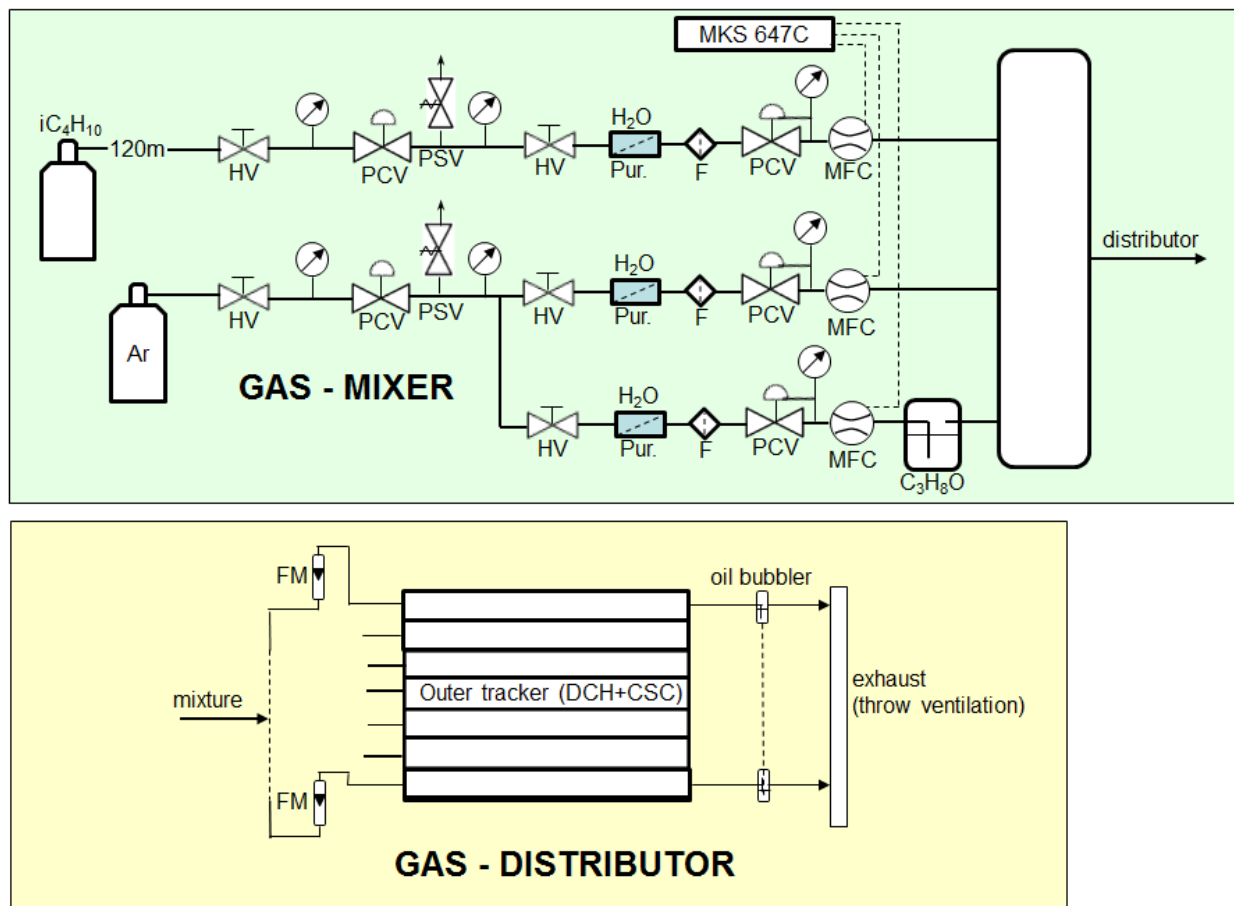


Fig. 29. The gas line for the Outer Tracker. At the top is shown the layout of the mixer module: HV – on/off valve, PCV – pressure control (constant) valve, PSV – pressure safety valve, Pur. – Purifier (H_2O and O_2), F – filter, MFC – mass flow controller, MKS 647C – power supply and readout. At the bottom is shown the component layout of the distributor module: FM – flowmeter (manual flow adjustment), oil bubbler – pressure and air protection.

555 **8. Forward Spectator Detectors**

556 Several detectors, which measure the energy or charge of the projectile spectators, are located at the very end of
557 the BM@N setup. These are the Forward Hadron Calorimeter (FHCAL), the Forward Quartz Hodoscope (FQH), and
558 the Scintillation Wall (ScWall). These detectors are used to determine the centrality of the collision and orientation
559 of the reaction plane. Moreover, the ScWall and FQH can also be used to study the charge distributions of charged
560 spectator fragments produced in nucleus-nucleus interactions.

561 *8.1. Forward Hadron Calorimeter*

562 The FHCAL has a granular structure in the transverse and longitudinal planes. It consists of 54 separate modules
563 in transverse plane (see Fig. 30). The internal part of the FHCAL consists of 34 small modules with transverse sizes
564 of $15 \times 15 \text{ cm}^2$ and a length equivalent to 4.0 nuclear interaction lengths. These modules are identical to the mod-
565 ules of the forward hadron calorimeters of the Multi-Purpose Detector (MPD) experiment at the NICA accelerator
566 complex [9]. Each of the two outer lateral parts of the calorimeter contains 10 larger modules with transverse size of
567 $20 \times 20 \text{ cm}^2$ and a length equivalent to 5.6 nuclear interaction lengths. These modules were initially constructed for
568 the hadron calorimeter of the Compressed Baryonic Matter (CBM) experiment (FAIR, Darmstadt, Germany) [10] and
569 are temporarily used in the BM@N experiment.

570 Beam ions pass that did not interact pass to a beam dump located behind the FHCAL through the hole in the center
571 of the calorimeter. The transverse size of the hole is $15 \times 15 \text{ cm}^2$. This design feature is dictated by the requirement
572 to protect internal modules and the front-end electronics of the FHCAL against the high radiation dose and strong
573 activation, typical for experiments with relativistic heavy ion beams.

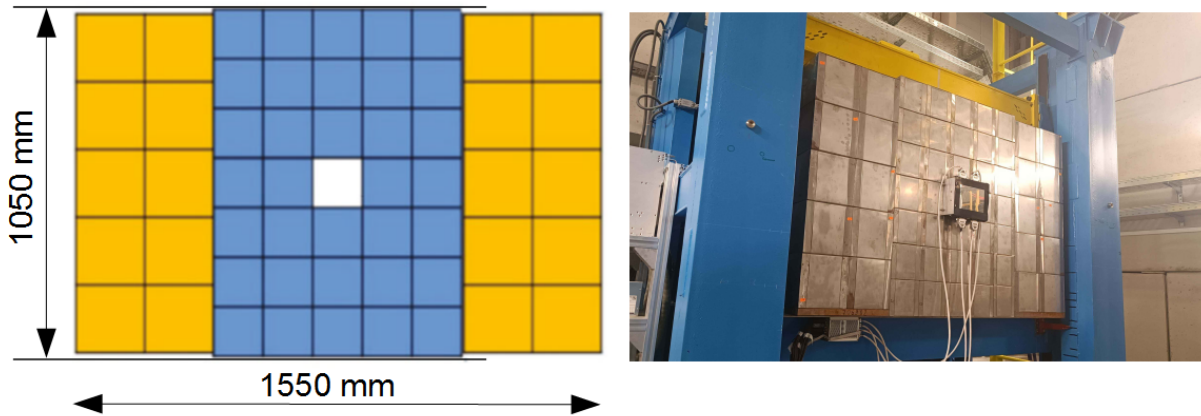


Fig. 30. Left: Schematic view of the FHCAL. Right: Photo of the FHCAL installed on the movable platform (blue) at BM@N.

574 The FHCAL modules have sampling structure and consist of lead/scintillator layers with a sampling ratio of 4:1
575 (the thickness of the lead plates and scintillator tiles is 16 mm and 4 mm , respectively) and fulfill the compensation
576 condition ($e/h = 1$) for the hadron calorimeter. The small modules have 42 lead/scintillator layers, while the large
577 modules have 60 such layers. To get rather high rigidity of the lead plates, they are made of lead-antimony alloy.
578 The assembly of 60 (42) alternating layers of scintillator and lead plates is bound into one package by a 0.5 mm
579 thick stainless steel band tightened using a special tensioning mechanism. After tightening, the tape is welded to
580 additional steel plates inserted at the beginning, in the middle and at the end of the module (Fig. 31). Behind the
581 tightening mechanism, a block of boron polystyrene with a thickness of 10 cm is installed in the large modules. Once
582 the package is assembled, it is closed by a cover box made of a 0.5 mm thick stainless steel sheet.

583 The scintillator plates are made of polystyrene-based plastic scintillator produced by Uniplast (Vladimir, Russia).
584 Light from the scintillator plates is collected by Kuraray Y11(200) wavelength shifting optical fiber glued into a
585 1.2 mm deep groove on the surface of the scintillation plate and transported to the end of the module. The grooves in

586 the scintillators of large modules have circular form, while those in the scintillators of small modules are spiral. The
 587 end of each fiber on the scintillator side is coated with reflective paint. After the fiber is glued in the scintillator plate,
 588 the plate is wrapped in a Tyvek reflector. Outside of the scintillator plate, the fibers are placed in thin black plastic pipes
 589 to be optically shielded. During the module assembly the plates are oriented in such a way that all optical fibers exit on
 590 the same side of the module (at the top). After that, groups of fibers from each of the six consecutive scintillation plates
 591 are glued into individual optical connectors (7 and 10 groups in the small and large modules, respectively), which are
 592 placed on a panel mounted on the rear side of the module box (see Fig. 31). Thus, each of the large modules has ten
 593 longitudinal sections, and each of the small modules has seven sections. The longitudinal segmentation provides high
 594 homogeneity of light collection along the modules, a large dynamic range of the calorimeter response, and makes it
 595 possible to perform detailed energy calibration of the FHCAL with cosmic muons [11].

596 The stability of the operation of the photodetectors and the calorimeter readout chain is controlled by a system
 597 of LEDs; one LED per calorimeter module. Correspondingly, the light from each LED is split to ten (seven) fibers,
 598 which are added into the optical connectors.

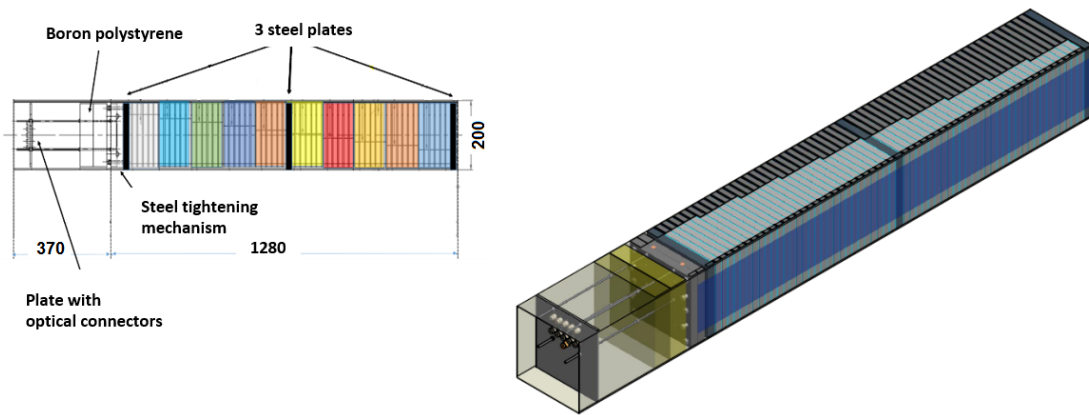


Fig. 31. Left: Scheme of a large calorimeter module, with 10 sections shown in different colors. Right: 3D view of an assembled large calorimeter module.

599 The weight of a single small and large module is about 200 kg and 500 kg, respectively. The total weight of the
 600 FHCAL is about 17 tons. The calorimeter is mounted on a special platform (Fig. 30, right), which is able to move the
 601 FHCAL in X and Y directions.

602 8.1.1. FHCAL photodetectors, FEE and readout electronics

603 The Hamamatsu S12572-010P MPPCs with a $3 \times 3 \text{ mm}^2$ sensitive area are used as photodetectors for light detection
 604 from the sections of the FHCAL. These photodetectors have a gain of 1.35×10^5 and a photon detection efficiency of
 605 about 10% at a peak sensitivity wavelength of 470 nm. Due to a very small pixel pitch ($10 \mu\text{m}$), the total number of
 606 pixels is 90 000, which is important for response linearity in a wide dynamic range of the signal. The FHCAL front-end
 607 electronics is composed of two separate PCBs. Ten (seven) photodetectors are installed on the first PCB directly
 608 coupled with light connectors at the end of each large (small) module. A temperature sensor is mounted near the
 609 photodetectors on an aluminum heat sink. The second PCB contains signal preamplifiers with differential ADC driver
 610 output and individually adjustable voltage regulation circuits for the photodetectors. This board also has an LED flash
 611 generation circuit with synchronization input. All FEE boards are remotely controlled via a specially designed HVSys
 612 System Module manufactured at JINR (Dubna, Russia).

613 The total number of FHCAL readout channels is 438. The digitization of signal waveforms is performed by eight
 614 ADC64s2 boards produced by AFI Eceltronics (JINR, Dubna, Russia). The boards have 64-channel 12-bit ADCs
 615 with a sampling rate of 62.5 MHz and a memory depth of up to 1024 points per channel. The ADC64s2 are capable
 616 of time synchronization via White Rabbit network, can operate in self-triggered or externally triggered modes, and
 617 digitize signals with or without zero suppression.

618 In addition to 438 signals from the individual longitudinal sections of the modules, the FEE boards provide 54
 619 summed signals, one for each calorimeter module. In order to operate with summed signals, a custom-made 12-
 620 channel analog fan-in electronic module with individually adjustable attenuation of input signals has been designed
 621 and manufactured at JINR. The fan-ins can be used to sum up the analog outputs from various groups of the FHCAL
 622 modules, if needed. One possible application of the fan-in modules is generation of a trigger signal based on energy
 623 deposition in either the whole FHCAL or in its “neutron” zone. In addition, the summed signals are used to provide
 624 trigger for cosmic calibration of the calorimeter modules.

625 8.1.2. FHCAL calibration with cosmic muons, energy resolution and linearity of the response

626 The energy calibration of the FHCAL is performed using cosmic muons. Longitudinal and transverse segmentation
 627 of the calorimeter allows reconstructing muon tracks [11] and accounting for track length variation in the scintillator
 628 tiles, depending on the track orientation. The distribution of signal amplitudes, corrected with the known muon
 629 track length, are fitted by a Landau distribution convoluted with a Gaussian. The MPV of the fit represents one
 630 MIP (minimum ionizing particle) response of the section. It can be characterized by the number of photoelectrons.
 631 Typically, the MIP response for individual sections corresponds to 40–50 photoelectrons.

632 A detailed study of the linearity of the response and energy resolution for an array of 9 large modules was per-
 633 formed using proton beams with a kinetic energy range of 1–9 GeV at the CERN T9 and T10 beamlines [15]. Good
 634 linearity and $0.54/\sqrt{E}$ energy resolution were obtained.

635 8.2. Forward Quartz Hodoscope

636 The FHCAL beam hole is covered with the FQH beam hodoscope. The main purpose of the FQH is to measure
 637 the charge of spectator fragments, which pass the beam hole of the calorimeter. In particular, the combined FHCAL
 638 and FQH response allows one to estimate the collision centrality [12]. The FQH consists of 16 quartz strips, which
 639 act as Cherenkov detectors. The size of the strips is $16 \times 1 \times 0.4 \text{ cm}^3$. The light from each FQH strip is viewed
 640 by two individual silicon photomultipliers mounted on both sides of the strip (see Fig. 32, right). The Hamamatsu
 641 S14160-3015PS MPPCs with a sensitive area of $3 \times 3 \text{ mm}^2$ and an efficiency of 32 % are used as photodetectors. The
 642 hodoscope strips with photosensors are placed inside a single light tight box (see Fig. 32, left).

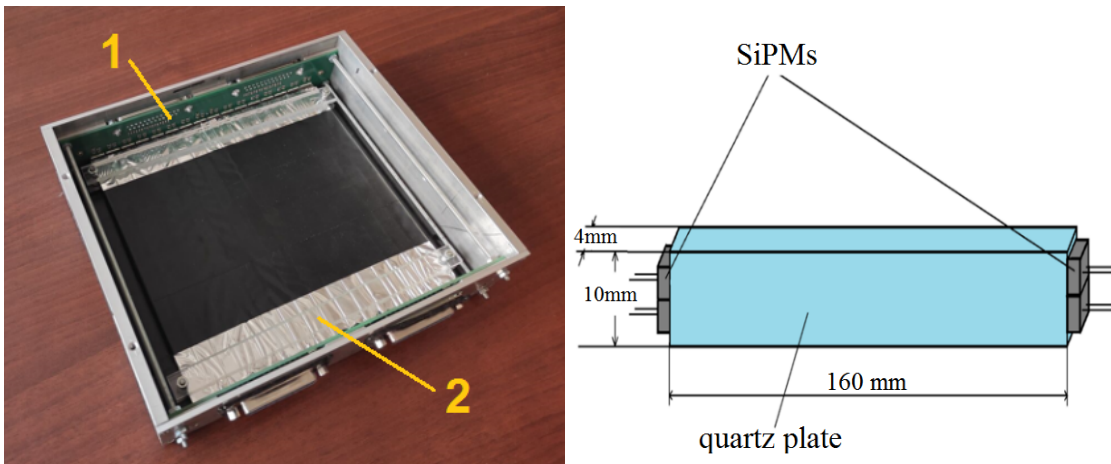


Fig. 32. Left: Photo of the Forward Quartz Hodoscope (inside view). 1 - the PCB with SiPMs, 2 - the quartz strips wrapped in reflective foils. Right: An FQH strip with SiPM photodetectors mounted.

643 Four FEE boards, each of which can process eight input signals, are used in the readout of the whole FQH. The
 644 FEE boards incorporate signal amplifiers with two-gain outputs, the gains being $1\times$ and $4\times$. The low gain channel
 645 is used to cover maximum dynamic range up to the highest ion charge expected. The high gain channel is used
 646 to measure the charge of low- Z fragments. Four TQDC-16 boards with a total of 64 channels are used to read out
 647 the two-gain outputs from each photodetector. Because the hodoscope is placed directly in the beamline, the charge

648 calibration of the FQH strips is performed with ion beam. The FQH strips were tested on the 280 MeV electron
649 beam of "Pakhra" synchrotron (LPI, Troitsk) and the light yield of about 5 photo-electrons on one MIP has been
650 observed [13].

651 8.3. Scintillation Wall

652 The ScWall is a large area detector aimed at measuring the charged particles in the forward rapidity region. It
653 consists of an array of scintillating plates placed in an aluminum box. A view of the ScWall is shown in Fig. 33. The
654 full detector size is $270 \times 130 \text{ cm}^2$. The ScWall has 40 inner small ($7.5 \times 7.5 \times 1 \text{ cm}^3$) scintillator detectors (cells) and
655 138 big outer cells ($15 \times 15 \times 1 \text{ cm}^3$). In order to avoid radiation damage caused by the heavy ion beam, as well as to
656 minimize background counts in other detectors, the very central part of the ScWall has a $15 \times 15 \text{ cm}^2$ beam hole (see
657 Fig. 33, right). The cells are made of polystirol-based scintillators manufactured by "Uniplast" (Vladimir, Russia).

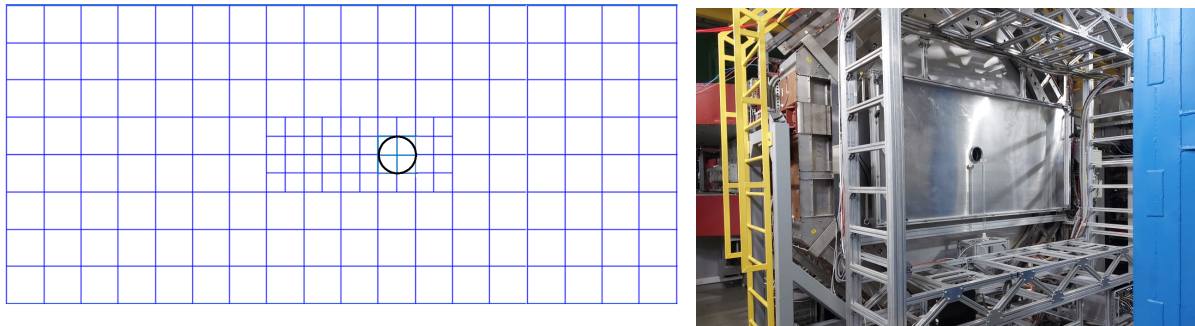


Fig. 33. Schematic view of the ScWall (left) and view of the ScWall detector with the beam hole mounted at the BM@N (right).

658 The light produced in the cells is collected by WLS Y11(200) S-type (Kuraray) wavelength shifting fibers embed-
659 ded in 1.5 mm deep grooves (see Fig. 34). At the end of the fibers, the light is detected by Hamamatsu S13360-1325CS
660 SiPMs, which have an active area of $1.3 \times 1.3 \text{ mm}^2$, a gain of 7×10^5 , and a photo detection efficiency of 25 %. The
661 light yield from a minimum ionizing particle passing the big and small cells is about 32 and 55 photoelectrons, respec-
662 tively [14]. The full area of the ScWall is divided into twelve readout zones. The readout is performed by ADC64s2
663 boards combined with FEE boards similar to the readout of the FHCAL signals. Three ADC64s2+FEE boxes are used
664 to digitize the signals from all the ScWall cells. Initial calibration of the ScWall channels is performed using cosmic
665 muons, and later verified and refined in the analysis of the experimental data using hits from particles with $Z = 1$
666 charge produced in the recorded events.

667 8.4. Slow Control for the forward detectors

668 As light sensors, the FHCAL, FQH and ScWall detector systems use SiPMs, whose amplification depends on tem-
669 perature and the applied bias voltage. Therefore a Slow Control (SC) system developed for these detectors monitors
670 the bias voltage (HV) and measures the temperature of the electronic boards with photodetectors. If needed, the
671 system automatically adjusts the HV based on temperature changes. The hardware part of the SC was designed and
672 manufactured by "HVSys" (JINR, Dubna, Russia). A schematic view of the system is shown in Fig. 35. Multichannel
673 HV power supply modules are operated via a microcontroller interface. Each HVSys module has a unique IP address
674 for communication through an individual proxy-server. The communication of the HVSys box with FEE microcon-
675 trollers is done via an RS-485 interface. All proxy-servers have connections to a GUI panel, which allows monitoring
676 the detector status and performing temperature correction for all SiPMs. The software part of the SC is written in
677 Python3 [16]. In order to record actual values of HV and temperature in a general database, the SC for the forward
678 detectors periodically relays this information to the main BM@N Slow Control System described in section 10.

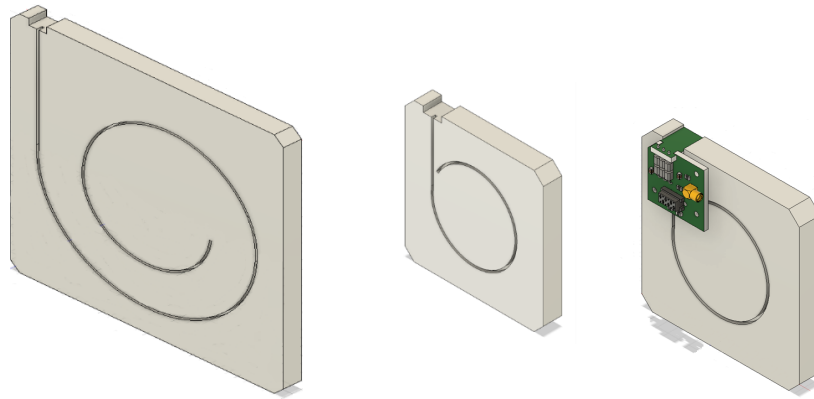


Fig. 34. Schematic view of the ScWall components: large cell (left), small cell (middle), assembly of a small cell with SiPM on a PCB with connectors (right).

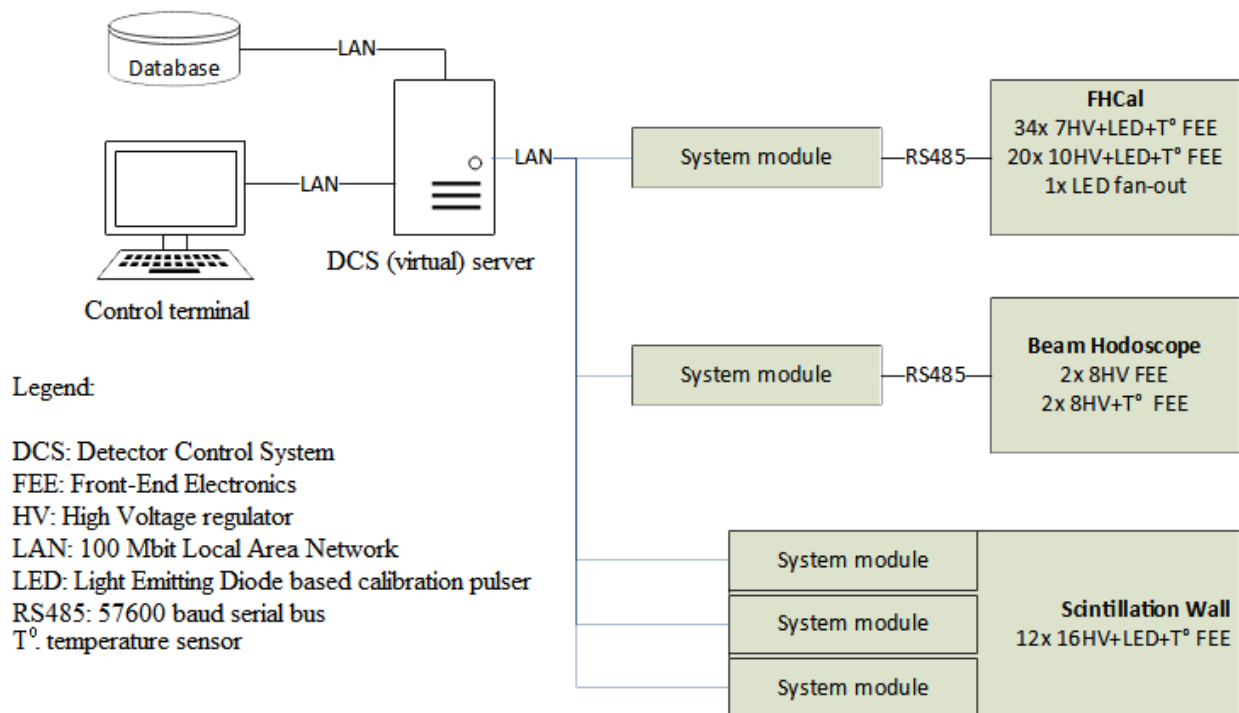


Fig. 35. Slow Control system for the forward detectors at BM@N.

679 9. Trigger and data acquisition

680 In the 2023 Xe run, the experiment operated at ~ 0.5 MHz beam intensity and most of the data were taken with a
681 2% interaction length target, resulting in an interaction rate ??????. Such conditions correspond to an interaction rate
682 of about 10 kHz, which exceeds the optimal DAQ event rate of a few kHz. Therefore, trigger settings were chosen to
683 ensure high efficiency for the most central and semi-peripheral collisions, while other types of events were added to
684 the readout with downscaling factors.

685 9.1. Trigger logic implementation

686 The BM@N trigger consists of hardware and software parts. The hardware part includes detectors based on fast
687 plastic scintillators described in section 3, low and high voltage power supply modules, and a programmable trigger
688 logic unit T0U. The software part includes a graphic trigger interface and programs, which control trigger performance
689 and beam quality.

690 The beam trigger (BT) is formed by the 20 ns pulse coincidence from the BC1, BC2 beam counters and the
691 absence of the pulse from the Veto counter (VC):

$$BT = BC1 \times BC2 \times \overline{VC}$$

692 The minimum bias trigger (MBT), in addition to the BT requirements, sets the criterion that only events with pulse
693 heights in the FD less than a preset threshold (below the beam ion peak) are considered as beam ion interactions in
694 the space between the BC2 and FD counters, i.e. primarily in the target:

$$MBT = BT \times \overline{FD}$$

695 The interaction trigger, called the Central Collision Trigger (CCT), is composed of the minimum bias trigger and
696 the signal from the Barrel Detector (BD) generated when the multiplicity of hits in the BD exceeds a certain threshold:

$$CCT = MBT \times BD(> N)$$

697 The logic of all the physics triggers mentioned above (BT, MBT, CCT) is implemented in a special custom-made
698 electronic module T0U, designed to accommodate the main tasks of the BM@N trigger (Fig. 36). The T0U has a
699 modular structure built on a motherboard that can be supplemented by mezzanine boards of four different types: four-
700 channel discriminator input cards, five channel FEE power supply, TTL-NIM convertor output cards, and Ethernet
701 interface card (ETB). The T0U accepts analog signals from the BC1, BC2, VC and FD counters, as well as the LVDS
702 pulses from the BD front-end electronics. Signal discrimination, delays and coincidence conditions are implemented
703 using FPGA functionality.

704 The trigger signals formed by the T0U are sent to the Trigger Distribution System, where they are processed with
705 corresponding downscaling factors.

706 9.2. Scalers

707 Trigger signals generated by the T0U are sent not only to the higher level trigger modules for further processing,
708 but also delivered to the MSC16VE 16-channel multihit scaler, which allows monitoring the trigger count rate during
709 data taking. Each channel input of the MSC16VE has 50 Ω impedance and accepts pulses of ± 2.5 V range. Dis-
710 crimination thresholds for input signals can be adjusted in a ± 1 V range. The module has four LVTTTL count enable
711 (CE) inputs. Data readout and module control are organized via Ethernet 1000BASE-X connection. The MSC16VE
712 module has three main logic parts: input part, multihit data readout and hardware histograms (Fig. 37).

713 The input part has a crosspoint switch that allows any input channel to be processed by any multihit counter and
714 histogram. CE and Gate logics have 16 independent Look-Up Tables (LUT) each. The Gate logic determines reset
715 conditions for hardware histograms. Multihit counters data are continuously subdivided into numbered time slices,
716 which are pushed to a data encoder and sent further to Ethernet. The length of time slices is adjustable with a minimum
717 of 64 ns and 8 ns increment. Data encoder performs zero suppression and data packing. The hardware histograms are
718 used for online monitoring of input counts in two possible forms: 1) count rate distribution in time, 2) time interval
719 between two adjacent hits. Both types of hardware histograms are available for online monitoring via GUI control
720 software.

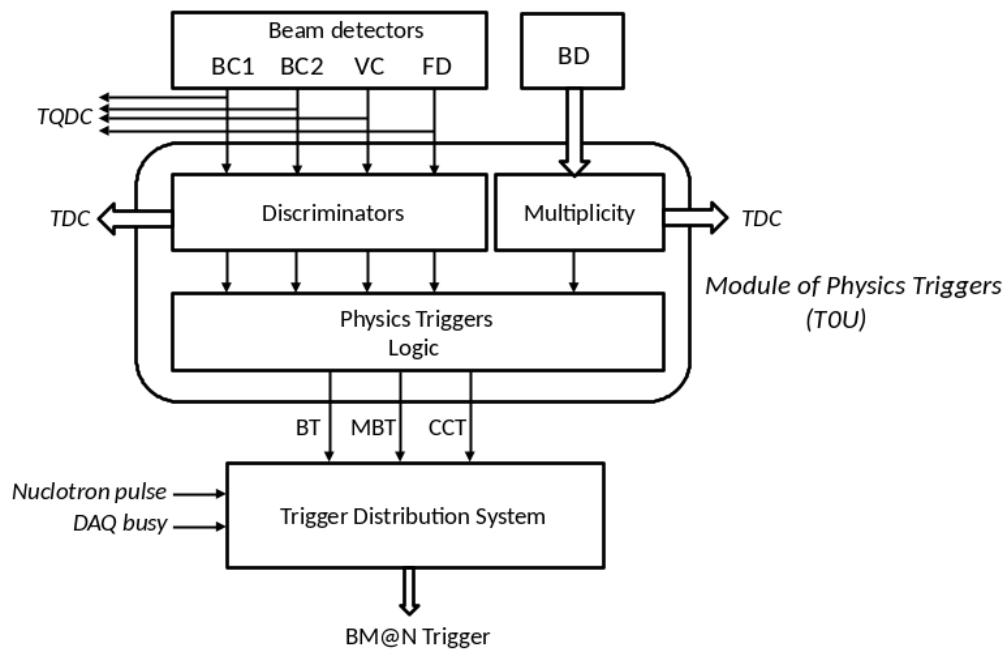


Fig. 36. Scheme of physics trigger generation in the TOU module.

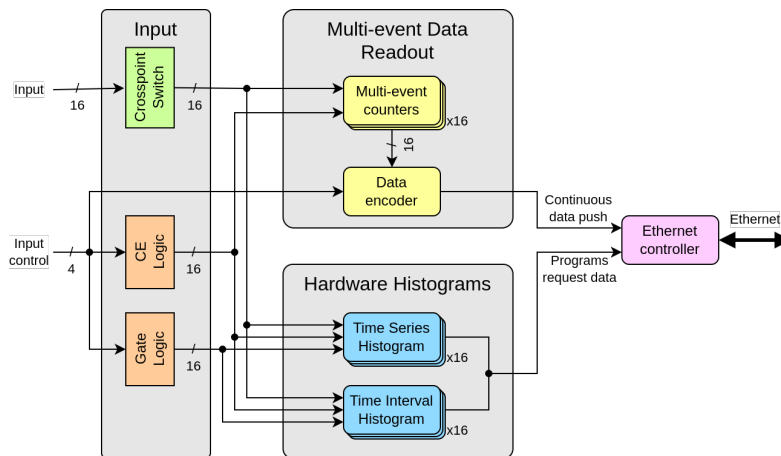


Fig. 37. MSC16VE module.

721 *9.3. General architecture of the trigger distribution system*

722 The BM@N trigger distribution system can accept up to 16 input triggers and process them at three levels of
 723 decision making: L0, L1 and L2 (Fig. 38). All signals in the trigger distribution system are transmitted via coaxial
 724 cables in the LVTTTL standard.

725 The L0 and L1 triggers are generated by a custom-made TRigger Control (TRC) module, which receives signals
 726 representing the physics driven triggers such as BT, CCT, MBT, etc., formed by the TOU. L0 is a fast signal produced

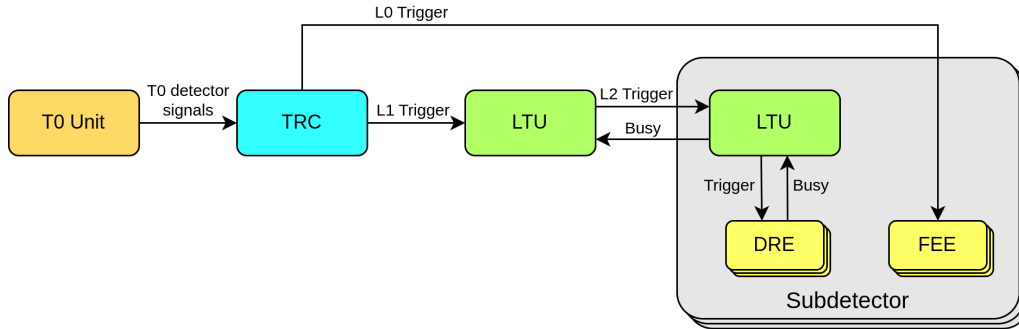


Fig. 38. BM@N trigger architecture.

727 with a typical latency of 300 ns and delivered to the front-end electronics of the tracking detectors (SiBT, FSD, GEM
 728 and CSC) as a trigger for sample holder circuits. L1 signals are trigger candidates derived from the physics triggers
 729 after applying downscaling factors. The formation time of the L1 trigger is adjustable and was set to $\sim 1\ \mu\text{s}$ in the
 730 2023 Xe run. In addition to the downscaling factor, each of the TRC input channels has individual settings adjustable
 731 by the user: signal delay and before/after protection time window. The before/after protection logic is used for pile-up
 732 event rejection. The output delays of L1 triggers can be set in the range from 8 ns to $100\ \mu\text{s}$. More than one L1 trigger
 733 can satisfy the downscaling conditions, the fastest of them is transferred to the Logical Trigger Unit (LTU), where the
 734 L2 trigger is generated and distributed. The LTU ensures the operation of the Trigger-Busy handshake algorithm and
 735 can process up to 16 busy channels. The Trigger-Busy handshake algorithm for the L2 trigger was implemented to
 736 guaranty the delivery of all triggers to the corresponding subsystems. This algorithm is shown in Fig. 39. The rising
 737 edge of the trigger signal (1) after a certain delay defines the start of the busy signal of a subsystem (2). After that the
 738 trigger signal is deasserted (3). Upon completion of data collection, the subsystem deasserts its busy signal (4).

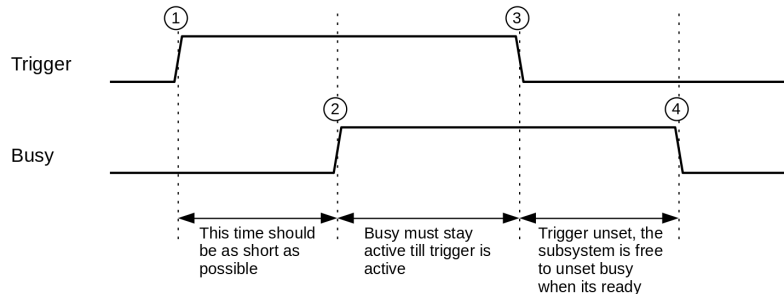


Fig. 39. Trigger handshake chronogram.

739 Busy signals can be received either from the detector readout electronics or from hierarchically lower LTU mod-
 740 ules. The time intervals between accepted triggers and the duration of the busy signals are histogrammed in the LTU
 741 internal memory. Various trigger counters are also implemented in the LTU module.

742 Typical busy time of the BM@N subsystems is shown in Fig. 40.

743 9.4. Detector readout data flow

744 The core function of the DAQ system is the realization of data transfer from detectors to the storage system. It
 745 includes the data flow from the readout electronics to the First Level Processor (FLP) fabric, to the Event Building
 746 (EvB) and to the Storage System. The main DAQ components are readout electronic modules, a clock and time
 747 synchronization system, data transfer networks, data processing servers and an online storage system. The general
 748 DAQ architecture and data flow are illustrated in Fig. 41.

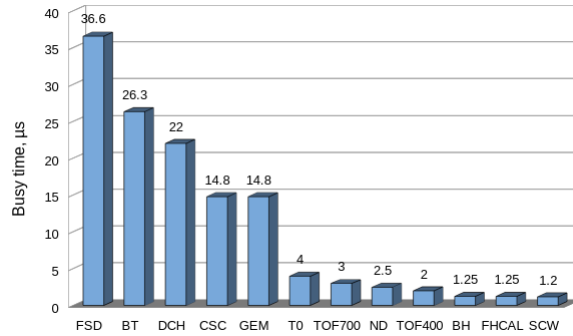


Fig. 40. The average busy time for all subsystems.

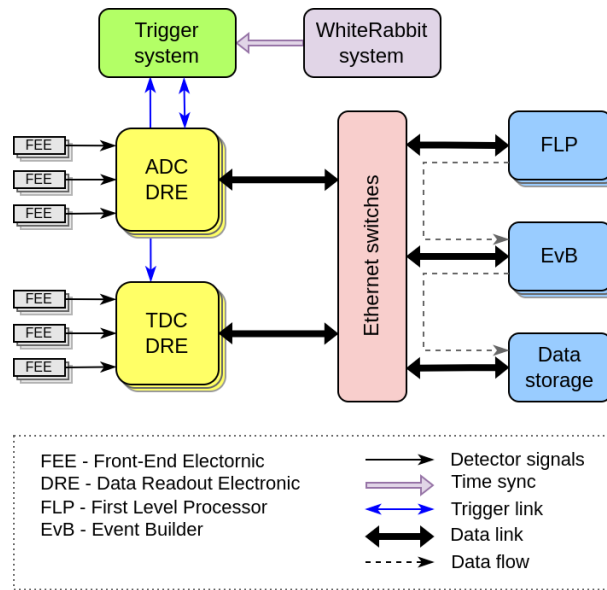


Fig. 41. General architecture of the DAQ system.

749 9.4.1. TDC and ADC boards

750 Detector Readout Electronic (DRE) boards record detector signals. BM@N has two main types of DRE boards
 751 grouped by function: time stamping in Time to Digital Converters (TDC) and amplitude sampling in Amplitude to
 752 Digital Converters (ADC). The TQDC DRE board combines both TDC and ADC functions.

753 The HPTDC based TDC DRE board performs timestamping of multiple discrete signals (hits) with typical accu-
 754 racy of 25 ps. Hit timestamps are kept for 51 μs in ring type memory. The total trigger latency should not exceed this
 755 value. The ADC DRE board is a waveform digitizer which samples an analogue input signal at fixed time intervals.
 756 It can be run in a zero suppression mode based on baseline estimation and signal threshold value. Signal shaping can
 757 be performed in digital form with FIR filters. It allows reducing the number of waveform points required for digital
 758 signal representation with minimum loss of accuracy. The ring type memory provides a possibility to read back the
 759 last 32 μs time window of digitized waveforms. This value sets the limit on the maximum trigger latency.

760 9.4.2. Timing synchronization system

761 Timestamping TDCs, which are used in the readout electronics of the trigger counter, TOF400 and TOF700
 762 detector systems, have a time resolution of 25 ps, while the DCH TDCs have a 100 ps resolution. These digitizer
 763 boards require precise reference clock for high quality measurements. They process signals using common notion

764 of time and frequency regulated by the White Rabbit network. The time reference is provided by a GPS/GLONASS
 765 receiver and backup precision frequency reference (Rubidium clock).

766 The White Rabbit ensures sub-nanosecond accuracy and picosecond precision of time synchronization for dis-
 767 tributed systems. The DRE boards include White Rabbit Node Core and tunable crystal oscillators that are synchro-
 768 nized to a reference clock with a 10 ps accuracy. The WR Node Core provides a local clock with a 125 MHz frequency
 769 and can set timestamps specified as TAI (International Atomic Time), which is an absolute number of seconds and
 770 nanoseconds since 01.01.1970. Frequency dividers synchronized by a 1 PPS (pulse per second) signal are used to
 771 produce digitizer clocks: 41.667 MHz for HPTDC ASICs and 62.5 MHz for the waveform digitizers.

772 9.4.3. DAQ data flow

773 All BM@N subdetectors, except the DCH, use Ethernet to transfer data from the readout electronics to the First
 774 Level Processors (FLP). The primary FLP task is to receive data stream in real time, buffer, validate, format and
 775 enqueue data blocks to an event building network. The FLP decouples the fast microsecond-scale synchronous data
 776 acquisition process from the slower, seconds-scale, software data processing by buffering the data in the computer
 777 RAM. The data transfer path from the readout electronic module to the event building network and storage system is
 778 shown in Fig. 42. for the typical 64-channel ADC based waveform digitizer module ADC64VE.

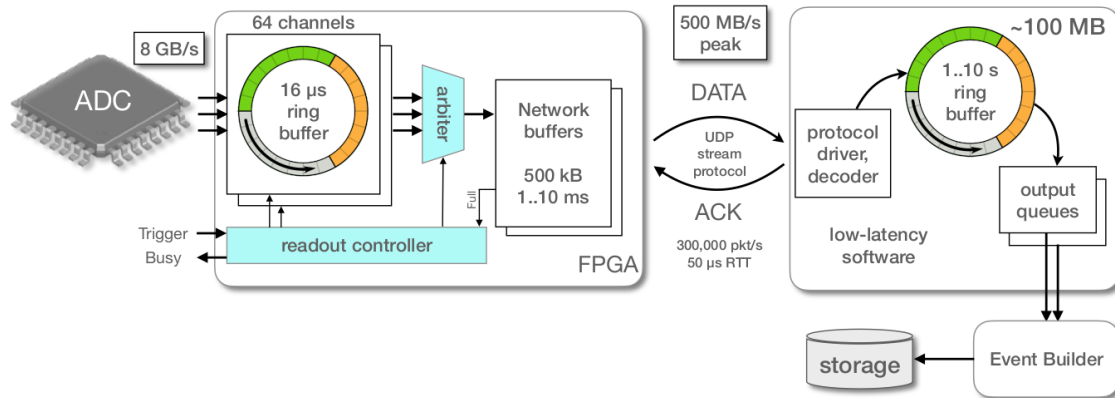


Fig. 42. Data flow from a detector to the storage system.

779 The electronic modules designed by the DAQ team share a common communication architecture. Network con-
 780 nectivity is provided by a hardware IP stack (HWIP), a programmable logic code synthesized for the onboard FPGA
 781 processor. Taking into account the limited memory and logic resources of FPGA chips available, and the implemen-
 782 tation complexity of the TCP protocol, a custom data transfer protocol MStream has been designed for data streaming
 783 over 1 Gb/s or 10 Gb/s Ethernet networks. It uses UDP over IP as the transport layer and implements an ordered and
 784 reliable data packet delivery using acknowledgments.

785 The FLP receives the data stream in real time. Dedicated servers with dual 18-core CPUs, equipped with dual
 786 100 Gb/s Ethernet adaptors, are running Fedora Linux OS. Tuning for real-time operation is necessary to ensure
 787 continuous data transfer without interruptions [27]. It includes the CPU frequency and supply voltage management,
 788 network adapter interrupt coalescence mitigation and system task scheduler adjustments.

789 The BM@N readout electronics deliver 6 GB/s raw data over 200 streams in peak at a 10 kHz trigger rate. A single
 790 data stream has a maximum sustained throughput of 500 MB/s when using 10 Gb/s Ethernet. Operation during the
 791 2023 Xe run showed that a single manually tuned FLP server was capable of hosting 10–12 data stream receivers with
 792 minimal contribution to overall busy time.

793 Software event building in BM@N is part of asynchronous processing and does not affect the readout busy time
 794 under normal operation. Event builders are cascaded in multiple layers for load distribution, and the last layer writes
 795 data files to the storage system.

796 Event builder programs associated with data intensive subdetectors run on dedicated hardware servers, while event
 797 builders for low data rate subdetectors, as well as readout control programs, run in a KVM virtual environment. This

798 allows efficient utilization of computer resources.

799 **9.5. DAQ storage system**

800 The DAQ server equipment is located in 4 racks of the modular data center (MDC). A total of 49 servers occupy
 801 81 units of rack space. Table 6 shows server types and functions.

Table 6. Characteristics of the BM@N DAQ server equipment.

Qty	Function	Specifications	Network
20	Compute node	Dual 18-core 3 GHz CPU, 384 GB RAM	Dual 100 Gb/s
10	NVMe storage server	10 × 3.5 TB NVMe	Dual 100Gb/s
8	HDD storage server 1	24 × 12 TB HDD, 1.8 TB SSD cache	Dual 100 Gb/s
4	HDD storage server 2	24 × 18 TB HDD, 3 TB SSD cache	Dual 100 Gb/s
6	Control server	4-core CPU, 64 GB RAM	Dual 25 Gb/s
1	Bootstrap server	4-core CPU, 16 GB RAM, 4 × 300 GB HDD	Dual 1 Gb/s

802 The core of the data network is a two-level Ethernet fabric with Clos architecture that has two switches on the
 803 spine level and multiple switches on the leaf level (Fig. 43). The Ethernet VPN (EVPN) virtualization technology
 804 is used to allow flexible traffic management, high availability and efficient link utilization. The underlay network
 805 provides connectivity between the fabric nodes. It is formed by leaf and spine switches connected with L3 routed
 806 links. The network topology is managed by the OSPF dynamic routing protocol. The overlay network that carries
 807 user traffic is realized with the MP-BGP protocol at the control plane and VXLAN encapsulation at the data plane.

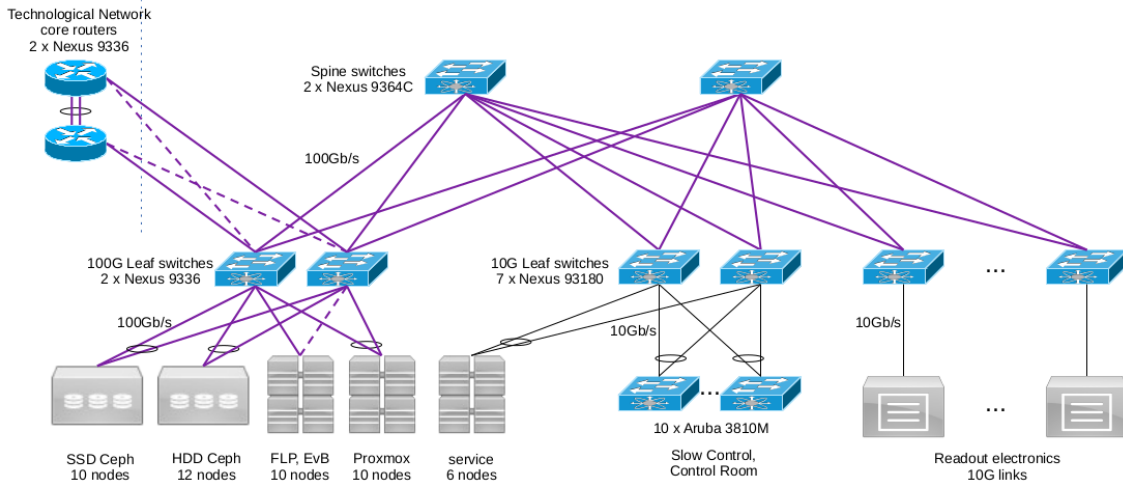


Fig. 43. BM@N DAQ Network.

808 The DAQ network supports jumbo Ethernet frames up to 9000 bytes to maximize throughput of data transfer from
 809 readout electronics. The network uses Any-Source Multicast that is necessary for automatic discovery of readout
 810 electronics modules and software components of the distributed DAQ system.

811 Two spine and four leaf switches are located in the MDC racks. Other leaf switches and access switches of slow
 812 control systems of various detectors are located in the electronics racks in the experimental area. Two core routers
 813 of the DAQ technological network are located in the experimental hall, close to the BM@N electronics. These routers
 814 provide connectivity to the outside network with a 200 Gb/s bandwidth.

815 The DAQ network showed no critical problems during BM@N data taking in the 2023 Xe run. The Ethernet
 816 switching fabric bandwidth proved to be adequate for peak traffic conditions and showed no negative impact on the

817 data taking performance. No significant packet drops or errors were registered by the monitoring system on network
818 fabric switches that could indicate network saturation and packet buffer overflows. The design of the DAQ network
819 takes into account a potential increase in both the trigger rate and event size in future experimental runs. If necessary,
820 the fabric bandwidth can be doubled by introducing an additional leaf to spine connections.

821 **10. Slow Control System**

822 The main objectives of the Slow Control System (SCS) include hardware status monitoring, archiving the opera-
 823 tional conditions of the facility, user-friendly graphical interface and alarm management system. The SCS was built
 824 around “TANGO Controls” [29], an open-source toolkit, widely used in scientific experiments.

825 Slow Control data from the experiment subdetectors such as: high voltage, low voltage, magnetic field, vacuum
 826 level, gas flow and mixture, etc. are aggregated by the SCS. These parameters are then stored in the TANGO Historical
 827 Database implemented using the PostgreSQL database with the TimescaleDB extension [30]. The SCS is configured
 828 as a distributed cluster with backup and load balancing.

829 The TANGO Database, which hosts the configuration of the whole system, and the TANGO Historical Database
 830 are running on the BM@N virtual machine cluster, whereas the programs controlling and/or monitoring the hardware
 831 status of a particular subsystem can run either on a virtual cluster or on a dedicated PC for this subsystem.

832 The user interface for online monitoring and retrieving previously stored data is developed with Grafana [31], an
 833 open-source analysis and interactive visualization web application. A schematic display of the experiment hardware
 834 status and alarms (Fig. 44) was also implemented using Grafana.

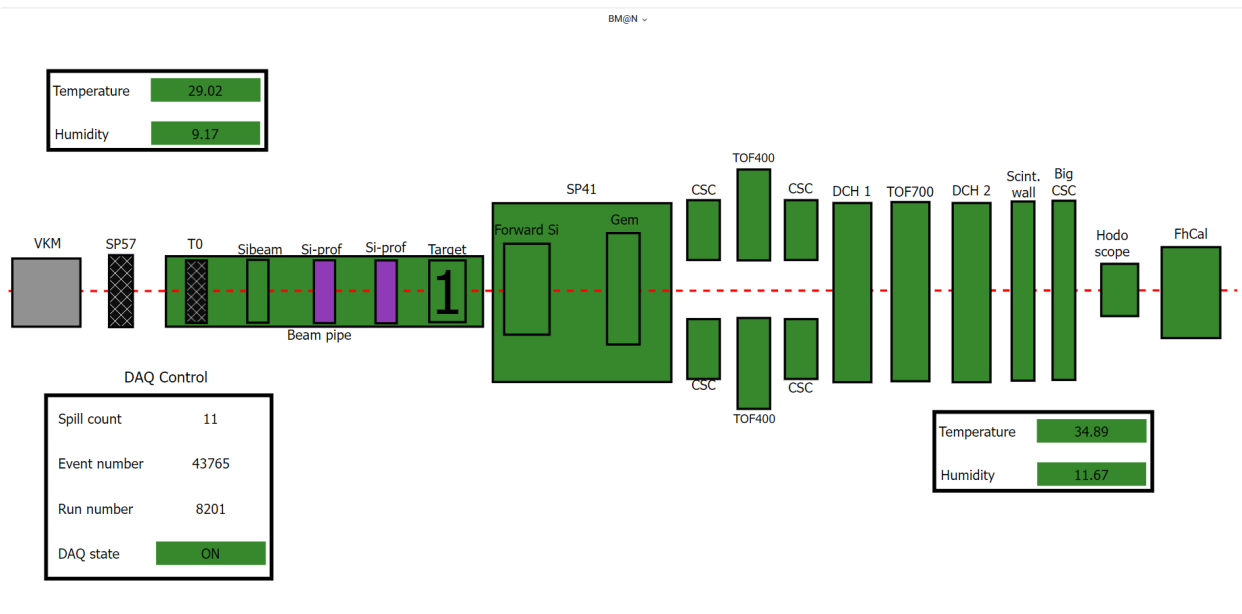


Fig. 44. Main display of the Slow Control System.

835 **11. Summary**

836 BM@N is a fixed target experiment recently put into operation at the Nuclotron/NICA complex aiming at the study
837 of nucleus-nucleus collisions at energies up to $4.5 \text{ GeV}/n$. The BM@N physics program is focused on the investigation
838 of properties of the baryonic matter with density 3–4 times higher than the nuclear saturation density. We presented
839 a detailed description of the BM@N spectrometer and its subsystems. The spectrometer design is driven by the
840 requirements to handle high beam intensity and high multiplicity of produced particles typical for central and semi-
841 central nucleus-nucleus collisions at relativistic energies. The major subsystems of the experiment include tracking
842 detectors capable to measure the momentum of produced particles in a wide rapidity interval, time-of-flight detectors
843 for charged particle identification, as well as forward spectator detectors designed to determine the centrality and the
844 reaction plane in each nucleus-nucleus collisions. The details of the trigger, data acquisition and control systems are
845 also described. The BM@N setup presented in this article corresponds to the configuration used in the 2023 Xe run.
846 During a three-week data taking period, about 0.4×10^9 Xe+CsI interaction events were collected at the beam energy
847 of $3.8 \text{ GeV}/n$. All the experiment subsystems operated at the expected level. A detailed evaluation of the detector
848 performance is ongoing. Further upgrade of some of the detector subsystems is foreseen, but the described setup is
849 close to the final configuration intended for experiments with heaviest (Au, Bi) beam ions.

850 **Acknowledgements**

851 The BM@N collaboration gratefully acknowledges the efforts of the staff of the accelerator division of the Labo-
852 ratory of High Energy Physics at JINR that made the data taking possible and successful. We appreciate the work done
853 by: V. Balandin (JINR), N. Kuzmin (JINR), A. Morozov (JINR), Yu. Petukhov (JINR), S. Sychkov (JINR), S. Vasiliev
854 (JINR), A. Vishnevsky (JINR)

855 **References**

856 [1] M. Kapishin (for the BM@N Collaboration), Studies of baryonic matter at the BM@N experiment (JINR) Eur. Phys. J. A52 no. 8 (2016)
857 213, <https://doi.org/10.1016/j.nuclphysa.2018.07.014>
858 [2] Needs to be updated.
859 [3] J. Randrup and J. Cleymans, Phys. Rev. C 74 (2006) 047901, <https://doi.org/10.1103/PhysRevC.74.047901>
860 [4] B. Friman, W. Nörenberg, and V.D. Toneev, The quark condensate in relativistic nucleus-nucleus collisions Eur. Phys. J. A 3 (1998) 165-170.
861 [5] NICA White Paper, Eur. Phys. J. A 52 (2016) 211 <https://doi.org/10.1140/epja/i2016-16211-2>
862 [6] BM@N Conceptual Design Report, http://nica.jinr.ru/files/BM@N/BMN_CDR.pdf
863 [7] Ch. Fuchs, Prog. Part. Nucl. Phys. 56 (2006) 1-103, <https://doi.org/10.1016/j.pnpnp.2005.07.004>
864 [8] P. G. Akishin *et al.*, Optimization of a large aperture dipole magnet for baryonic matter studies at Nuclotron, Phys. Part. Nuclei Lett. 12 (2015)
865 305-309, <https://doi.org/10.1134/S154747711502003X>
866 [9] A. Ivashkin *et al.*, <http://mpd.jinr.ru/doc/mpd-tdr/> 2017
867 [10] F. Guber *et al.*, Technical Design Report for the CBM Projectile Spectator Detector (PSD) - GSI-2015-02020,
868 <http://repository.gsi.de/record/109059/files/20150720> 2015
869 [11] A. Izvestnyy *et al.*, Calibration of FHCAL with cosmic muons at the BM@N experiment, J. Phys. Conf. Ser. 1690 (1) (2020) 012060, <https://doi.org/10.1088/1742-6596/1690/1/012060>
870 [12] F. Guber *et al.*, Measurements of Centrality in Nucleus–Nucleus Collisions at the BM@N Experiment, Phys.Part.Nucl. 52 (2021) 4, 571-577,
871 <https://doi.org/10.1134/S1063779621040262>
872 [13] A.G. Baranov *et al.*, The Amplitude Parameters of Prototypes of the Forward Hodoscopes for the BM@N Experiment, Instrum.Exp.Tech. 64
873 (2021) 3, 352-356, <https://doi.org/10.1134/S0020441221020111>
874 [14] A.G. Baranov *et al.*, Measurement of the Parameters of the Forward Scintillator Wall of the BM@N Experiment, Instrum.Exp.Tech. 65 (2022)
875 1, 42-46, <https://doi.org/10.1134/S002044122201002X>
876 [15] N. Karpushkin *et al.*, Study of the hadron calorimeters response for CBM and BM@N experiments at hadron beams, Journal of Physics
877 Conference Series 1667(1):012020 <https://doi.org/10.1088/1742-6596/1667/1/012020>
878 [16] O. Petukhov, S. Morozov, Development of Detector Control System (DCS) for forward hadron calorimeters in the BM@N and the MPD
879 experiments, J.Phys.Conf.Ser. 1690 (2020) 1, 012063, <https://doi.org/10.1088/1742-6596/1690/1/012063>
880 [17] D. Baranov *et al.*, GEM tracking system of the BM@N experiment, 2017 JINST 12 C06041, [https://doi.org/10.1088/1748-0221/](https://doi.org/10.1088/1748-0221/12/06/C06041)
881 [12/06/C06041](https://doi.org/10.1088/1748-0221/15/09/C09038)
882 [18] A. Galavanov *et al.*, Status of the GEM/CSC tracking system of the BM@N experiment, 2020 JINST 15 C09038, [https://doi.org/10.](https://doi.org/10.1088/1748-0221/15/09/C09038)
883 [1088/1748-0221/15/09/C09038](https://doi.org/10.1051/epjconf/201920407009)
884 [19] A. Galavanov *et al.*, Performance of the BM@N GEM/CSC tracking system at the Nuclotron beam, EPJ Web Conf. 204 07009 (2019),
885 <https://doi.org/10.1051/epjconf/201920407009>
886 [20] F. Anghinolfi *et al.*, NINO: An ultra-fast and low-power front-end amplifier/discriminator ASIC designed for the multigap resistive plate
887 chamber, Nucl.Instrum.Meth.A 533 (2004) 183-187, <https://doi.org/10.1016/j.nima.2004.07.024>
888 [21] M.G.Buryakov *et al.*, Status of the front-end electronics for the time-of-flight measurements in the MPD experiment, Phys.Part.Nucl.Lett. 13
889 (2016) 532, <https://doi.org/10.1134/S1547477116050058>
890 [22] N.A.Kuzmin *et al.*, High-rate glass MRPC for fixed target experiments at Nuclotron, Nucl.Instr.Meth.A 916 (2019) 190-194, [https://doi.](https://doi.org/10.1016/j.nima.2018.11.098)
891 [org/10.1016/j.nima.2018.11.098](https://doi.org/10.1016/j.nima.2015.11.060)
892 [23] J. Christiansen, HPTDC High Performance Time to Digital Converter, CERN, Geneva, 2004, Version 2.2 for HPTDC version 1.3.
893 [24] V. Babkin *et al.*, Triple-Stack Multigap Resistive Plate Chamber with Strip Readout, Nucl.Instr.Meth.A 824 (2016) 490-492, [http://dx.](http://dx.doi.org/10.1016/j.nima.2015.11.060)
894 doi.org/10.1016/j.nima.2015.11.060
895 [25] D. Bédérède *et al.*, High resolution drift chambers for the NA48 experiment at CERN Nucl. Instr. and Meth. A 367 (1995) 88-91, [https://doi.org/10.1016/S0168-9002\(95\)00637-0](https://doi.org/10.1016/S0168-9002(95)00637-0)
896 [26] I. Augustin *et al.*, The Drift chamber electronics and readout for the NA48 experiment, Nucl. Instr. and Meth. A 403 (1998) 472, [https://doi.org/10.1016/S0168-9002\(97\)01128-5](https://doi.org/10.1016/S0168-9002(97)01128-5)
897 [27] RedHat, Optimizing RHEL 9 for Real Time for low latency operation, [https://access.redhat.com/documentation/en-us/red_](https://access.redhat.com/documentation/en-us/red_hat_enterprise_linux_for_real_time/9)
898 [hat_enterprise_linux_for_real_time/9](https://access.redhat.com/documentation/en-us/red_hat_enterprise_linux_for_real_time/9)
899 [28] S. Weil *et al.*, Ceph: A Scalable, High-Performance Distributed File System. OSDI 1906: 7th USENIX Symposium on Operating Systems
900 Design and Implementation, Pp. 307-320 of the Proceedings. <https://ceph.com/assets/pdfs/weil-ceph-osdi06.pdf>
901 [29] Tango is an Open Source solution for SCADA and DCS, <https://www.tango-controls.org>
902 [30] PostgreSQL is a powerful, open source object-relational database, <https://www.postgresql.org>
903 [31] Grafana is a multi-platform open source analytics and interactive visualization web application, <https://grafana.com>
904
905
906